

On Dispersive and Classical Shock Waves in Bose-Einstein Condensates and Gas Dynamics

M. A. Hoefer,^{1,*} M. J. Ablowitz,¹ I. Coddington,² E. A. Cornell,^{2,†} P. Engels,^{2,‡} and V. Schweikhard²

¹*Department of Applied Mathematics, University of Colorado,
Campus Box 526, Boulder, Colorado 80309-0526*

²*JILA, National Institute of Standards and Technology and University of Colorado,
and Department of Physics, University of Colorado, Boulder, Colorado 80309-0440, USA*

(Dated: February 6, 2008)

A Bose-Einstein condensate (BEC) is a quantum fluid that gives rise to interesting shock wave nonlinear dynamics. Experiments depict a BEC that exhibits behavior similar to that of a shock wave in a compressible gas, eg. traveling fronts with steep gradients. However, the governing Gross-Pitaevskii (GP) equation that describes the mean field of a BEC admits no dissipation hence classical dissipative shock solutions do not explain the phenomena. Instead, wave dynamics with small dispersion is considered and it is shown that this provides a mechanism for the generation of a dispersive shock wave (DSW). Computations with the GP equation are compared to experiment with excellent agreement. A comparison between a canonical 1D dissipative and dispersive shock problem shows significant differences in shock structure and shock front speed. Numerical results associated with the three dimensional experiment show that three and two dimensional approximations are in excellent agreement and one dimensional approximations are in good qualitative agreement. Using one dimensional DSW theory it is argued that the experimentally observed blast waves may be viewed as dispersive shock waves.

I. INTRODUCTION

It is well known that a shock wave in a compressible fluid is characterized by a steep jump in gas velocity, density, and temperature across which there is a dissipation of energy due fundamentally to collisions of particles. The aim of this article is to present experimental and numerical evidence of a different type of shock wave which is generated in a quantum fluid that is a Bose-Einstein condensate (BEC). In this case, the shock front is dominated not by dissipation but rather dispersion. Viewed locally, these dispersive shock waves (DSWs) with large amplitude oscillations and two associated speeds bear little resemblance to their classical, dissipative counterparts. However, we demonstrate that a direct comparison is possible when one considers a mean field theory, corresponding to the *average* of a DSW.

Since extensive theoretical work has been done in the field of compressible gas dynamics (cf. [1]), it is important to relate this work to the “dispersive gas dynamics” which BEC embodies. The present work contrasts and compares dissipative and dispersive shock waves through multidimensional numerical simulation and analytical studies. We also provide an explanation of what a BEC shock wave is in the context of the well understood concept of a classical shock wave in gas dynamics.

Early experiments studying shock-induced dynamics

in BEC were reported in [2] where a slow-light technique was used to produce a sharp density depression in a BEC. Direct experimental imaging of BEC blast waves has been performed in the rotating context and numerical solutions of the governing Gross-Pitaevskii (GP) equation were used to describe the wave dynamics [3]. Theoretical studies of the zero dissipation limit of classical gas dynamics as applied to BEC was discussed in [4, 5] where it was shown that a shock wave could develop. Subsequently, in [6] the shock wave in the small dispersion limit of the one dimensional repulsive GP equation was analyzed using the Whitham averaging method and the attractive GP equation was analyzed in [7].

In the present paper, for the first time a comparison between dissipative and dispersive shock waves is carried out through a careful investigation of new experiments and theory in one, two, and three dimensions.

The outline of this work is as follows. In section I A we give the relevant dynamical equation, i.e. the GP equation, and we put it in non-dimensional form and give the associated conservation laws. In section II we present new experimental results depicting “blast” waves in a non-rotating BEC. In section III we show that direct three dimensional numerical simulations, with radial symmetry using the GP equation give excellent agreement with these experiments. In section IV an analysis of dissipative and dispersive shock waves in two types of one-dimensional systems, the inviscid Burgers’ equation and the Euler equations, is provided. Two types of limiting behavior for conservation laws, the *dissipative regularization* (small dissipation limit) and *dispersive regularization* (small dispersion limit) are considered. We then present numerical evidence showing that the three dimensional and two dimensional calculations agree extremely well (less than one percent relative difference). It is also

*Electronic address: hoefer@colorado.edu

†Also at Quantum Physics Division, National Institute of Standards and Technology

‡Present address: Department of Physics and Astronomy, Washington State University, Pullman, WA 99163

found that the one dimensional approximation of the 3D blast wave experiments is in good qualitative agreement. Using one dimensional theory, we explain why the experimentally observed blast waves may be viewed as DSWs.

A. Gross-Pitaevskii and the Navier-Stokes Equations

An analogy between the classical equations of fluid flow, the Navier-Stokes (NS) equations, and the density, phase equations for the wave function (order parameter) associated with a BEC is well known [8]. The crucial difference from NS is a dispersive term that replaces the dissipative term in classical fluid dynamics.

The GP equation models the mean-field dynamics of the BEC wave function Ψ and has been shown to be an effective approximation in many situations. Experiments in rapidly rotating BECs have provided evidence of dynamics similar to what is often considered to be “blast waves”. Moreover, simulations with the Gross-Pitaevskii equation were compared with experiment giving support to the validity of the GP equation in such extreme circumstances [3].

The dimensional GP equation is [8]

$$i\hbar\Psi_t = -\frac{\hbar^2}{2m}\nabla^2\Psi + V_0\Psi + NU_0|\Psi|^2\Psi, \quad (\text{I.1})$$

with conservation of particle number

$$\int_{\mathbb{R}^3} |\Psi|^2 d^3x = 1. \quad (\text{I.2})$$

The coefficient of nonlinearity, $NU_0 = N4\pi\hbar^2 a_s/m$, is characterized by the inter-particle scattering length a_s (here positive representing repulsive particles) and the number of condensed atoms N ; the other parameters are the atomic mass of the species considered (m) and Planck’s constant divided by 2π (\hbar). The standard confining harmonic potential (trap) is given by

$$V_0(x, y, z) = \frac{m}{2} (\omega_\perp^2 (x^2 + y^2) + \omega_z^2 z^2),$$

where ω_\perp and ω_z are the radial and axial trap frequencies respectively. A convenient normalization for our purposes is to take [9]

$$t' = \omega_\perp t, \quad \vec{x}' = \frac{\vec{x}}{l}, \quad \Psi' = l^{\frac{3}{2}} \Psi, \quad l = \left(\frac{4\pi\hbar^2 |a_s| N}{m^2 \omega_\perp^2} \right)^{\frac{1}{5}}.$$

After dropping primes, equation (I.1) becomes

$$i\varepsilon\Psi_t = -\frac{\varepsilon^2}{2}\nabla^2\Psi + V_0\Psi + |\Psi|^2\Psi, \quad (\text{I.3})$$

where

$$\varepsilon = \left(\frac{\hbar}{m\omega_\perp (4\pi a_s N)^2} \right)^{\frac{1}{5}} \ll 1,$$

with the normalization of the wavefunction (I.2) preserved and the trap potential

$$V_0(r, z) = \frac{1}{2}(r^2 + \alpha_z z^2), \quad r^2 = x^2 + y^2.$$

The coefficient $\alpha_z = (\omega_z/\omega_\perp)^2$ represents the asymmetry in the harmonic trap. In the experiments considered, the parameters are: $N = 3.5 \cdot 10^6$ particles, $a_s = 5.5$ nm and $m = 1.45 \cdot 10^{-25}$ kg for the species ^{87}Rb , $(\omega_\perp, \omega_z) = 2\pi(8.3, 5.3)$ Hz, and $\alpha_z = 2.45$. This normalization shows that the dispersion is extremely small, $\varepsilon = 0.012$.

Conservation of “mass” and “momentum” for the GP equation (I.3) are,

$$\frac{d}{dt} \int_{\mathbb{R}^3} |\Psi|^2 d\vec{x} = 0, \quad \frac{d}{dt} \int_{\mathbb{R}^3} (\Psi^* \nabla \Psi - \Psi \nabla \Psi^*) d\vec{x} = 0. \quad (\text{I.4})$$

Since it will be useful for later discussions, we give the local conservation laws in the 1D case (see e.g. [10])

$$\begin{aligned} \rho_t + (\rho u)_x &= 0 \\ (\rho u)_t + (\rho u^2 + \frac{1}{2}\rho^2)_x &= \frac{\varepsilon^2}{4}(\rho(\log \rho)_{xx})_x - \rho V_x, \end{aligned} \quad (\text{I.5})$$

where subscripts denote differentiation. The condensate “density” ρ and “velocity” u are defined by

$$\Psi = \sqrt{\rho} e^{i\phi/\varepsilon}, \quad u = \phi_x.$$

Equations (I.5) give an alternative formulation of the GP equation in terms of “fluid-like” variables. Since the ε^2 term is obtained from the linear dispersive term in eq. (I.3), we call this the dispersive term.

The Navier-Stokes equations for a 1D compressible gas with density ρ and velocity u can be written [11]

$$\begin{aligned} \rho_t + (\rho u)_x &= 0 \\ (\rho u)_t + (\rho u^2 + P)_x &= \varepsilon^2 u_{xx} + \rho F, \end{aligned} \quad (\text{I.6})$$

where P is the pressure and F is an external force per unit mass. The positive coefficient ε^2 represents dissipative effects due to viscous shear and heat transfer. If the pressure law

$$P = \frac{1}{2}\rho^2$$

is assumed (for example, a perfect, isentropic gas with adiabatic constant $\gamma = 2$ or, equivalently, the shallow water equations for height ρ and velocity u), then the NS equations (I.6) correspond to the GP conservation equations (I.5) when $\varepsilon^2 = 0$ and $F = -V_x$. Equations (I.6) for the case $\varepsilon^2 = 0$ and $F = 0$ are called the Euler equations. To compare different types of shock waves, we are interested in the dispersive regularization ($\varepsilon^2 \rightarrow 0$ in (I.5)) as compared to the dissipative regularization ($\varepsilon^2 \rightarrow 0$ in (I.6)) of the Euler equations ($V_x = F = 0$).

A remark regarding the form of the above equations. Many authors use the velocity form

$$\rho_t + (\rho u)_x = 0$$

$$u_t + \left(\frac{1}{2}u^2 + \rho\right)_x = \frac{\varepsilon^2}{4\rho}(\rho(\log \rho)_{xx})_x - V_x,$$

of equation (I.5) by implicitly assuming differentiability and that $\rho \neq 0$. As we will be interested in *weak*, hence not everywhere smooth, solutions to the dissipative regularization of the Euler equations, it is necessary to maintain the form of the conservation laws as derived directly from the original integral formulation (I.4). It is well known that weak solutions to different forms of the same conservation law can be quite different. One must also be careful when dealing with the vacuum state $\rho = 0$ as in classical gas dynamics. The momentum equation (I.5) takes both of these issues into account.

II. EXPERIMENT

In order to investigate the fundamental nature of shock waves in a quantum fluid, we have performed new experiments that involve blast pulses in BECs. In contrast to the experiments described in [3], the experiments analyzed in this work are all done with non-rotating condensates. We have succeeded in directly imaging dispersive shock waves in these systems, and the particular geometry of these experiments makes them amenable to the theoretical analysis presented in this paper.

Condensates consisting of approximately 3.5 million Rb atoms were prepared in an axisymmetric trap with trapping frequencies of $(\omega_\perp, \omega_z) = 2\pi(8.3, 5.3)$ Hz; ω_\perp is the radial frequency and ω_z is the axial frequency. After the condensate was formed, a short, tightly focused laser beam was pulsed along the z -axis through the center of the BEC. The wavelength of the laser was 660 nm, which is far red-detuned from the Rb transitions. The pulse rapidly pushes atoms from the center of the BEC radially outward, leading to the formation of a density ring. Before imaging, an anti-trapping technique was used to enlarge the features of the blast wave. In brief, a rapid expansion of the BEC is created by changing the internal state of the atoms such that they are radially expelled by the strong magnetic fields forming the trap. Details about the anti-trapped expansion are described in [12]. While the anti-trapped expansion changes the scale of the features involved, it does not alter the qualitative appearance of the shock phenomena, as is confirmed by our numerical simulations.

A sequence of five images taken at the end of experimental runs with different laser pulse intensities is shown in Fig. 1(a-e). For this sequence, a 5 ms long pulse was sent through the BEC center directly before the start of a 50 ms long anti-trapped expansion. The laser waist was 13.5 microns. For comparison, the diameter of the

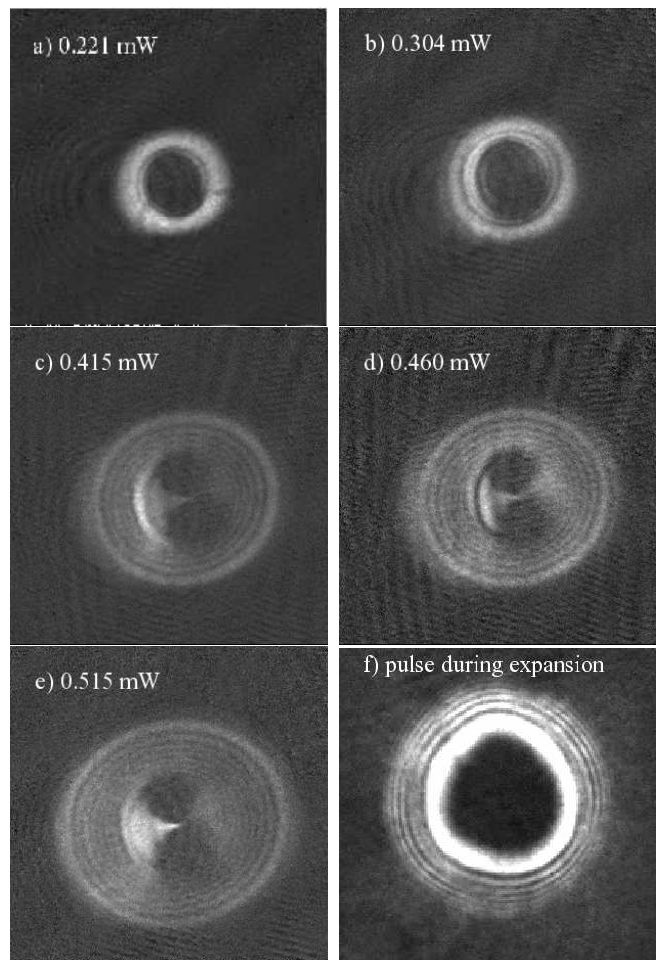


FIG. 1: Absorption images of blast pulse experiments with a BEC. a-e) Pulse applied before expansion. f) Pulse applied during expansion.

BEC in the radial direction was approximately 65 microns. The laser power is given in the images. All images were taken at the end of the anti-trapped expansion along the z -axis, which is also the direction of the blast pulse. For weak blast pulse intensities (Fig. 1a,b), essentially one broad ring of high density is seen, which is due to the fact that the laser pulse has pushed atoms radially outwards. When the blast pulse intensity is increased, a system of many concentric rings appears (1c-e).

The outcome of a second type of experiment is shown in Fig. 1f. By pulsing the blast laser during (instead of before) the anti-trapped expansion, we can image a situation where the compressional ring has not run through the condensate yet. For this image, a 5 ms long pulse with a power of 1.9 mW and a beam waist of 20 microns was used, starting 9.2 ms after the beginning of a 55 ms long anti-trapped expansion. In this case, an oscillatory wave structure is seen on the outside of the compressional ring. The analytical discussion together with the numerical studies presented in this paper reveal that for both experiments the oscillatory wave structure

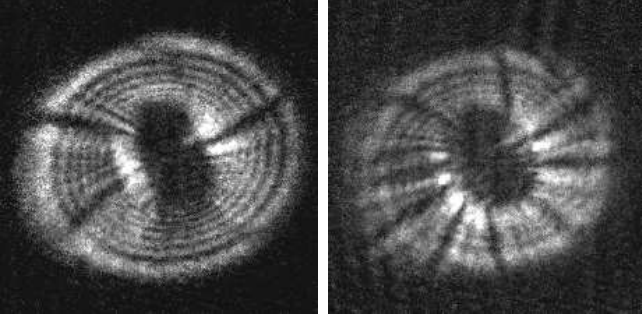


FIG. 2: Two examples of experiments with blast pulses in slowly rotating BECs.

is a direct consequence of dispersive shock waves which are fundamentally different from classical shock waves.

Finally, we note that the peculiar wedge shaped appearance of the central BEC region in Fig. 1(c-e) is due to a slight, unavoidable deviation of the laser beam shape from cylindrical symmetry. This asymmetry also leads to the slightly elliptical appearance of the whole BEC in these images.

By using rotating instead of static condensates, we can also observe an intriguing alteration of the blast wave pattern. Blast wave images in slowly rotating BECs are shown in Fig. 2. Upon slow rotation, dark radially directed spokes appear in the condensate, cutting through the ring shaped pattern familiar from the non-rotating case. The number of these spokes increases with increasing rotation rate, so it is suggestive to attribute them to the presence of vortices in the rotating BEC. We speculate that the spokes come about when vortices are present in the compressional ring formed by the blast. As this ring expands and forms the concentric ring system, the density depressions of the vortices are not filled in due to the predominantly radial expansion of the compressional ring. In rapidly rotating BECs, the presence of strong Coriolis forces lead to a rather different appearance of blast waves. The rapidly rotating situation was discussed in [3].

III. SIMULATIONS

We have performed direct numerical simulations of the GP equation (I.3), modeling the two types of experiments without rotation explained in the previous section.

The two experiments depend on when the laser is pulsed. We refer to these cases as either in trap (*it*) or out of trap (*ot*) and model them by the following time

varying potentials respectively

$$V_{it}(r, z, t) = \begin{cases} \frac{1}{2}(r^2 + \alpha_z z^2) & t < 0 \\ \frac{1}{2}(r^2 + \alpha_z z^2) + \frac{P_{it}}{d_{it}^2} e^{-r^2/d_{it}^2} & 0 \leq t \leq \delta t \\ \frac{1}{2}(-\alpha_r r^2 + \alpha_z z^2) & \delta t < t \end{cases} \quad (\text{III.1})$$

$$V_{ot}(r, z, t) = \begin{cases} \frac{1}{2}(r^2 + \alpha_z z^2) & t < 0 \\ \frac{1}{2}(-\alpha_r r^2 + \alpha_z z^2) & 0 \leq t \leq t_* \\ \frac{1}{2}(-\alpha_r r^2 + \alpha_z z^2) + \frac{P_{ot}}{d_{ot}^2} e^{-r^2/d_{ot}^2} & t_* \leq t \leq t_* + \delta t \\ \frac{1}{2}(-\alpha_r r^2 + \alpha_z z^2) & t_* + \delta t < t. \end{cases} \quad (\text{III.2})$$

The in trap potential (III.1) models a steady state solution held in trap while a Gaussian laser pulse is applied for the time δt . After the laser pulse, a radial anti-trap potential is applied [12]. This models the experiments shown in Fig. 1(a-e). For the out of trap potential (III.2) (modeling Fig. 1f), a steady state solution is expanded radially. At the time t_* , a Gaussian laser pulse is applied with duration δt followed by continued radial expansion. The Gaussian laser has width d and intensity proportional to P . The out of trap potential has the effect of generating an outward, radial velocity in the BEC before the laser pulse is applied whereas the in trap potential does not.

Modeling the non-rotating experiments presented in the previous section gives the parameter values: $t_* = 0.48$ (9.2 ms), $\delta t = 0.26$ (5 ms), $\alpha_r = 0.71$ (frequency of inverted harmonic potential used for expansion $2\pi \cdot 7$ Hz), and $\alpha_z = 0.57$.

The steady state solution is approximated well by the Thomas-Fermi wavefunction [8], a balance between the harmonic trapping potential and nonlinearity. However, its use numerically gives rise to unphysical oscillations. Therefore, we used an iterative technique similar to the technique discussed in [13] to find the precise, smooth 3D solution of the GP equation. We provide a brief outline of the method here.

Assume a stationary solution of the form

$$\Psi(\vec{x}, t) = e^{-i\mu t/\epsilon} \phi(\vec{x}) \quad (\text{III.3})$$

where μ is the normalized condensate chemical potential. Inserting the ansatz (III.3) into equation (I.3) and taking its Fourier transform (denoted by $\widehat{}$) gives

$$(\mu - \frac{1}{2}\epsilon^2|\vec{k}|^2)\widehat{\phi} = \widehat{V_0}\widehat{\phi} + \widehat{|\phi|^2\phi} \equiv \widehat{F}(\phi), \quad (\text{III.4})$$

where \vec{k} is the Fourier wave vector. Equation (III.4) suggests the iteration

$$\widehat{\phi}_{n+1} = \frac{\widehat{F}(\phi_n)}{\mu - \frac{1}{2}\epsilon^2|\vec{k}|^2}.$$

For $\mu > 0$, the denominator is singular when $|\vec{k}|^2 = 2\mu/\varepsilon^2$. Also, the normalization (I.2) is not conserved by this scheme. Therefore, we introduce the modified iteration scheme

$$\begin{aligned}\hat{\phi}_{n+\frac{1}{2}} &= \frac{\hat{F}(\phi_n) + c\hat{\phi}_n}{\mu - \frac{1}{2}\varepsilon^2|\vec{k}|^2 + c}, \\ \hat{\phi}_{n+1} &= \frac{\hat{\phi}_{n+\frac{1}{2}}}{\sqrt{\int_{\mathbb{R}^3} |\hat{\phi}_{n+\frac{1}{2}}|^2 d^3k}}, \\ \mu_{n+1} &= \int_{\mathbb{R}^3} \left(\frac{\varepsilon^2}{2} |\vec{k}|^2 \hat{\phi}_{n+1} + \hat{F}(\phi_{n+1}) \right) (\hat{\phi}_{n+1})^* d^3k.\end{aligned}\quad (\text{III.5})$$

The positive constant c is introduced by adding $c\hat{\phi}$ to both sides of equation (III.4). The chemical potential, μ , is updated along with the mode ϕ by integrating equation (III.4), with $\hat{\phi} = \hat{\phi}_{n+1}$, multiplied by $(\hat{\phi}_{n+1})^*$. This scheme preserves the normalization condition (I.2). Given an initial guess ϕ_0 and a large enough value for c (we took $c = 1.75$), we find that the scheme (III.5) converges to a 3D ground state wavefunction $\phi(\vec{x})$ for the GP equation. This is a general, fast method for finding the 3D BEC ground state for arbitrary potentials V_0 .

The condensate is evolved according to a pseudo-spectral Fourier code with a standard 4th order Runge-Kutta time stepper. Radial spatial derivatives are approximated by taking the fast Fourier transform of Ψ in the radial direction r evenly extended ($\Psi(-r, z, t) = \Psi(r, z, t)$) and then multiplying by ik (k is the Fourier wavenumber). The result is then inverted using the inverse fast Fourier transform giving a fast, spectrally accurate approximation to Ψ_r [14]. The Ψ_{zz} term is approximated similarly. The specific, model equation (I.3) assumes cylindrical coordinates with axial symmetry: $\nabla^2 \equiv \frac{\partial^2}{\partial r^2} + \frac{1}{r} \frac{\partial}{\partial r} + \frac{\partial^2}{\partial z^2}$. In the simulations, we used the laser width as an effective fitting parameter. We found that by taking the width, d , to be 1.5 times larger than its experimental value in the in trap case, excellent results were obtained. For the out of trap case, the laser width was taken to be half its experimental value, also giving excellent results.

First we consider the in trap case corresponding to the potential (III.1). A plot of the evolution of the condensate as a function of radial distance is shown in Fig. 3. On the left is the normalized density as given by the square modulus of the wavefunction plotted in the $z = 0$ plane $|\Psi(r, z = 0, t)|^2$. On the right is the phase gradient $\frac{\partial}{\partial r} \arg \Psi(r, z = 0, t)$ or radial velocity in the $z = 0$ plane. The normalized laser width and power used were $d_{it} = 0.41$ and $P_{it} = 0.70$ (corresponding to a laser waist of $20 \mu\text{m}$ and a power of 0.46 mW as in Fig. 1d).

Fig. 3 describes the following evolution. The condensate forms a high density ring ($t = 0$ to $5 \text{ ms} = \delta t$ in non-dimensional form) due to the applied laser pulse. When the ring is steep enough ($t = 7.5 \text{ ms}$), oscillations develop on the inner side of the ring ($t = 10 \text{ ms}$). This

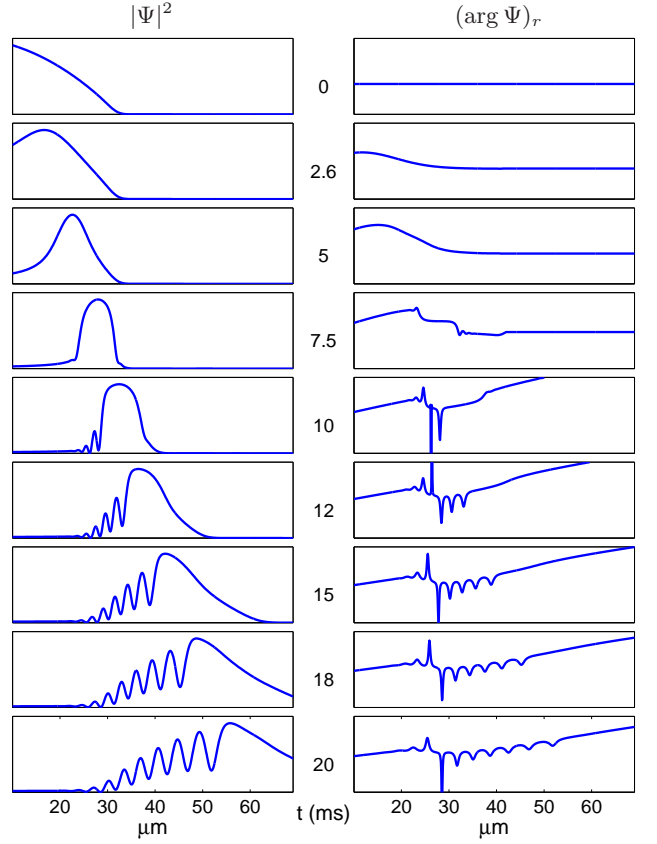


FIG. 3: BEC density evolved as in the in trap experiment. On the left is the density $|\Psi(r, 0, t)|^2$ and on the right is the radial velocity $\frac{\partial}{\partial r} \arg \Psi(r, 0, t)$; both are imaged in the $z = 0$ plane. The density scale is not constant throughout the sequence; in each frame, the density is scaled to its largest value so that the dispersing wave is visible. A high density ring forms accompanied by oscillations on its inner side, a DSW. This DSW expands and propagates outward. Note the time is in the center. All figures depicting a time evolution of the condensate in this work follow the same form as this figure.

oscillatory region expands radially due to the inversion of the trap potential to an anti-trap potential. The expansion continues until time $t = 55 \text{ ms}$ when an image is taken to compare with experiment (Fig. 4).

In Fig. 4, we show that the numerical simulation and the in trap experiment presented in the previous section (Fig. 1d) are in good qualitative agreement. The condensate features at $t = 20 \text{ ms}$ in Fig. 3 expand due to atomic repulsion and the anti-trap potential giving the contour plot of the density at $t = 55 \text{ ms}$ (corresponding to the end of the experiment) in Fig. 4. The experimental picture 1d is reproduced in Fig. 4 left for convenience. The simulation used all nominal values for parameters except the laser waist (d in non-dimensional units) which was taken to be $20 \mu\text{m}$ rather than the experimental value of $13.5 \mu\text{m}$. We speculate that the difference might be due to the slight deviation of the experimental beam profile from a perfect Gaussian, as indicated by the asymmetry

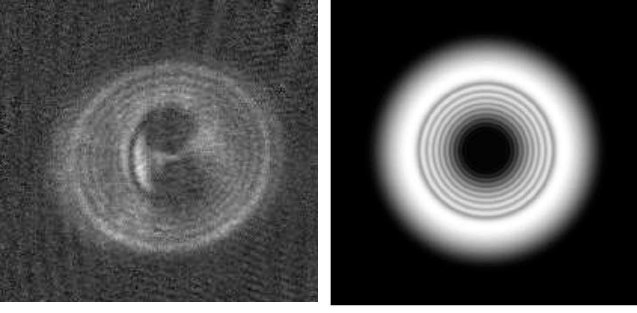


FIG. 4: Comparison of the condensate density from the in trap experiment (left) and numerical simulation (right) using the potential V_{it} , equation (IV.7). The image from simulation is a contour plot of the function $\int |\Psi(r, z, t)|^2 dz$, modeling the experimental imaging process where the photo was taken along the z axis. Both the simulation and experimental pictures were taken at $t = 55$ ms. The approximate diameter of the condensate cloud from simulation is $850 \mu\text{m}$ and from experiment is $775 \mu\text{m}$.

of the central regions in Fig. 1.

Next we consider the out of trap case corresponding to the potential V_{ot} (III.2). A plot of the evolution of the condensate in the $z = 0$ plane as a function of radial distance r is shown in Fig. 5. Initially, the condensate expands in the radial direction due to the anti-trap potential ($t = 0$ to 9.2 ms or $t = t_*$ in normalized units). A ring of high density forms while the laser is on ($t = 10$ ms), similar to the previous in trap case. When the steepness of this ring is large enough, oscillations start to develop on the inner *and* outer sides of the ring ($t = 10.2$ ms). These two oscillatory regions expand, quickly overlapping one another, giving rise to more complicated *multi-phase* type behavior with a propagating wave front that continues out radially ($t \geq 10.4$ ms). This behavior is due to the initial velocity imparted to the condensate by the anti-trap potential. The normalized laser width and power were $d_{ot} = 0.21$ and $P_{ot} = 2.88$ corresponding to a laser waist of $10 \mu\text{m}$ (half the experimental value of $20 \mu\text{m}$) and a power of 1.9 mW.

In Fig. 6, we show that the numerical simulation of the out of trap experiment presented in the previous section (Fig. 1f) show good qualitative agreement. For this comparison, the numerically determined condensate density is shown at the time $t = 18.0$ ms, the result of continued expansion from the state at the bottom of Fig. 5. The experimental picture was taken at $t = 55$ ms.

The rest of this paper is concerned with understanding the oscillatory structures that developed in Figures 3 and 5 as we will argue that they are dispersive shock waves with the oscillations in the latter Figure caused by the interaction of two DSWs.

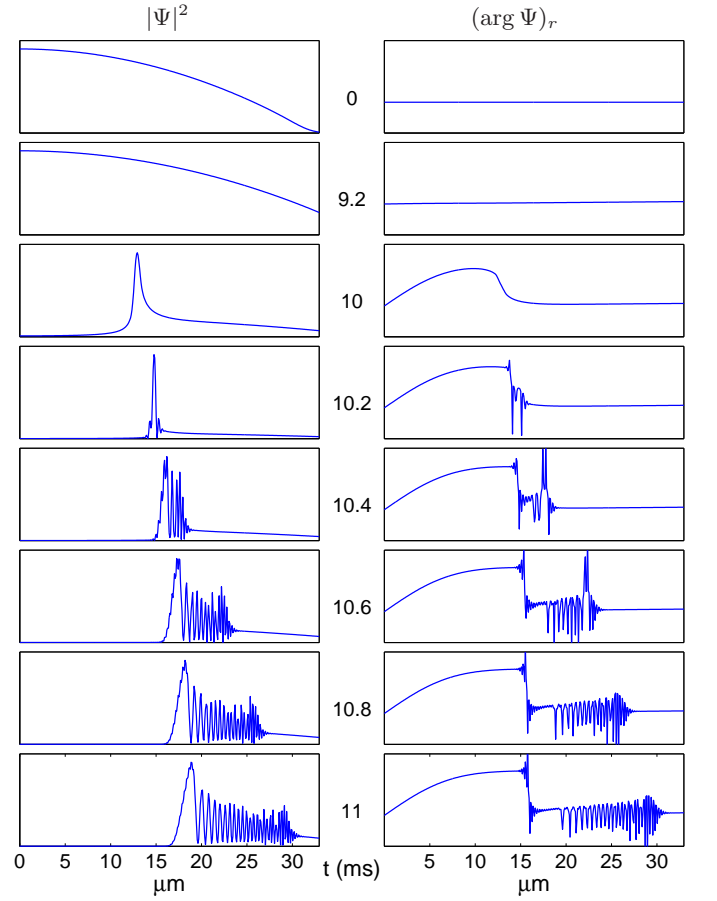


FIG. 5: BEC density evolved as in the out of trap experiment. On the left is the density and on the right is the radial velocity, both imaged in the $z = 0$ plane. A high density ring forms accompanied by oscillations on its inner and outer sides, two DSWs. These DSWs quickly interact and propagate outward.

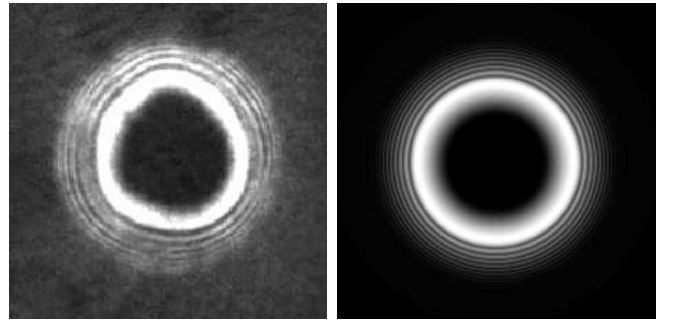


FIG. 6: Comparison of the condensate density from the out of trap experiment (left) and numerical simulation using the potential V_{ot} (III.2) (right). The image from simulation is a contour plot of the function $\int |\Psi(r, z, t)|^2 dz$, modeling the experimental imaging process. The approximate diameter of the condensate cloud from simulation is $116 \mu\text{m}$ and from experiment is $363 \mu\text{m}$.

IV. CLASSICAL AND DISPERSIVE SHOCK WAVES

In this section, the notions of classical shock waves and dispersive shock waves are discussed. We provide a theoretical basis for the experimental and numerical results presented in the previous sections. Using the classical gas dynamics analogy, it is shown that shocks in a BEC are fundamentally different from those in the classical case. The analytical methods to understand classical shocks and DSWs in one dimension are presented along with explicit results for DSW speeds and shock structure. Finally, detailed numerical investigations in 1D, 2D, and 3D are presented to show that the qualitative behavior of a DSW in 3D is captured by the 1D case and that the experiments presented earlier do give rise to DSWs.

We begin by studying the simplest nonlinear dissipative and dispersive equations that, under a suitable limit, give rise to shock waves, the Burgers and Korteweg-deVries equations. This provides a foundation to understand the differences between dissipative and dispersive shocks. The theory of classical shock waves is well developed (cf. [1, 15, 16]) so we will give only a brief synopsis suitable for comparison with the much less developed dispersive shock wave case.

A. Classical Shock Waves, Burgers' Equation

The classical dissipative shock in one dimension is modeled by Burgers' equation

$$u_t + \left(\frac{1}{2}u^2\right)_x = \varepsilon^2 u_{xx}, \quad (\text{IV.1})$$

where ε^2 is a measure of the dissipation and u represents, for example, a density. Equation (IV.1) admits traveling wave solutions with a hyperbolic tangent profile (see Fig. 7)

$$u(x, t; \varepsilon) = \frac{1}{2} + \frac{1}{2} \tanh \left\{ -\frac{1}{4\varepsilon^2} \left(x - \frac{1}{2}t \right) \right\}. \quad (\text{IV.2})$$

The speed of this wave is $v_c = 1/2$, independent of ε . In the limit $\varepsilon \rightarrow 0$, the (smooth) \tanh profile converges pointwise to the discontinuous function

$$\lim_{\varepsilon \rightarrow 0} u(x, t; \varepsilon) = u(x, t) = u(x/t) = \begin{cases} 1 & x/t < \frac{1}{2} \\ 0 & x/t > \frac{1}{2} \end{cases}. \quad (\text{IV.3})$$

The above formula is a mathematical description of a classical shock wave. The limiting process $\varepsilon \rightarrow 0$, $\varepsilon \neq 0$, in equation (IV.1) is a *dissipative regularization* of the conservation law

$$u_t + \left(\frac{1}{2}u^2\right)_x = 0. \quad (\text{IV.4})$$

The initial value problem (IVP) for equation (IV.4) with the initial data

$$u(x, 0) = \begin{cases} 1 & x < 0 \\ 0 & x > 0 \end{cases}, \quad (\text{IV.5})$$

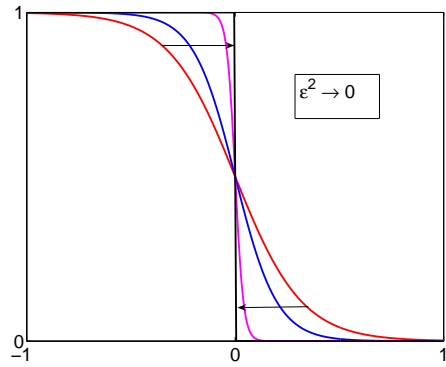


FIG. 7: Dissipative Burgers' equation shock solution (IV.2) with $\varepsilon^2 \rightarrow 0$, converging to a traveling discontinuity or classical shock wave.

is not well posed because the spatial derivative u_x is undefined at the origin. To see this, note that equation (IV.4) shows that a wave $u(x, t)$ propagates with a speed equal to the value of u at that point. Initially, for $x < 0$, the speed is 1 whereas for $x > 0$, the speed is 0 so u will *break* or become multi-valued at the origin for any $t > 0$. The classical theory of shock waves remedies this problem by considering *weak solutions* and invoking a *jump* or Rankine-Hugoniot condition at a discontinuity which relates the value of u on the left (u_l) and the right (u_r) to the speed v of the shock wave. A weak solution $u(x, t)$ for the conservation law (IV.4) satisfies the integral formulation

$$\frac{d}{dt} \int_a^b u(x, t) dx + \frac{1}{2} (u(b, t)^2 - u(a, t)^2) = 0, \quad (\text{IV.6})$$

for any a, b such that $-\infty < a < b < \infty$, thus allowing discontinuities in $u(x, t)$ as a function of x . The jump condition for Burgers' equation, derived from (IV.6) assuming a uniformly traveling discontinuity with values u_l and u_r to the left and right of the discontinuity respectively, is $v = (u_l + u_r)/2$ or $v = \frac{1}{2}$ for the initial data (IV.5), which is exactly the speed of the Burgers shock (IV.2). This simple example suggests that finding the dissipative regularization of (IV.4) (equation (IV.1) with $\varepsilon^2 \rightarrow 0$) is equivalent to solving the conservation law (IV.4) with the jump condition $v = (u_l + u_r)/2$ at each discontinuity. Indeed, this is generally true, assuming the entropy condition $u_l > u_r$ is satisfied [15].

When the entropy condition at a discontinuity is not satisfied, $u_l < u_r$, a shock wave solution is not appropriate. The correct choice is a rarefaction wave which is continuous for $t > 0$. Assuming that the solution depends on the self-similar variable $\xi = x/t$, equation (IV.4) becomes

$$u'(u - \xi) = 0. \quad (\text{IV.7})$$

Solutions to (IV.7) are constants or $u(x, t) = x/t$, the latter corresponding to a rarefaction wave. Then the weak solution for initial data $u(x, 0) = 0$, $x < 0$,

$u(x, 0) = 1, x > 0$ is

$$u(x, t) = u(x/t) = \begin{cases} 0 & x/t < v^- \\ \frac{x}{t} & v^- < x/t < v^+ \\ 1 & v^+ < x/t \end{cases} \quad (\text{IV.8})$$

This rarefaction wave has two associated speeds v^- and v^+ : $v^- = 0$ at the interface between the constant left state $u = 0$ and the self-similar solution $u = x/t$ and $v^+ = 1$ at the interface between the constant right state $u = 1$ and the self-similar solution $u = x/t$.

The general case of a system of conservation laws is written

$$\vec{u}_t + (\vec{F}(\vec{u}))_x = 0,$$

where \vec{u} is a vector “density” and \vec{F} is the vector “flux”. The IVP for this n -dimensional system with constant step initial data $\vec{u}(x, 0) = \vec{u}_l, x < 0$ and $\vec{u}(x, 0) = \vec{u}_r, x > 0$, assuming a dissipative regularization, is called a Riemann problem (note that the jump is specified at $x = 0$). The jump condition at a shock with speed v is

$$v(\vec{u}_r - \vec{u}_l) = \vec{F}(\vec{u}_r) - \vec{F}(\vec{u}_l). \quad (\text{IV.9})$$

It is well known (see e.g. [15]) that the solution to the Riemann problem, assuming certain properties of the flux \vec{F} , is self-similar consisting of $n + 1$ constant states “connected” by shock waves or rarefaction waves. That is

$$\vec{u}(x/t) = \begin{cases} \vec{u}_0 & x/t < v_1^- \\ \vec{w}_1(x/t) & v_1^- < x/t < v_1^+ \\ \vec{u}_1 & v_1^+ < x/t < v_2^- \\ \vdots & \vdots \\ \vec{w}_n(x/t) & v_n^- < x/t < v_n^+ \\ \vec{u}_n & v_n^+ < x/t \end{cases}, \quad (\text{IV.10})$$

where each \vec{u}_i is constant and $\vec{w}_i(x/t)$ represents a shock or rarefaction wave solution. The Lax entropy condition necessary for the existence of the shock wave \vec{w}_i is [17]

$$\begin{aligned} \lambda_i(\vec{u}_{i-1}) &> v_i^- = v_i^+ \equiv v_i > \lambda_i(\vec{u}_i), \\ \lambda_k(\vec{u}_{i-1}) &< v_i \quad \text{and} \quad \lambda_k(\vec{u}_i) < v_i \quad k < i, \\ \lambda_k(\vec{u}_{i-1}) &> v_i \quad \text{and} \quad \lambda_k(\vec{u}_i) > v_i \quad k > i. \end{aligned} \quad (\text{IV.11})$$

A shock wave \vec{w}_i has one speed of propagation so the $2i^{\text{th}}$ inequality in (IV.10) is replaced by $x = v_i t$. The λ_i in (IV.11) are the eigenvalues of the matrix with entries at (i, j)

$$\left(\frac{\partial F_i(\vec{u})}{\partial u_j} \right),$$

numbered so that $\lambda_1 < \lambda_2 < \dots < \lambda_n$. In addition to the entropy condition for the i^{th} wave \vec{w}_i to shock, the jump condition (IV.9) is satisfied for $v = v_i, \vec{u}_l =$

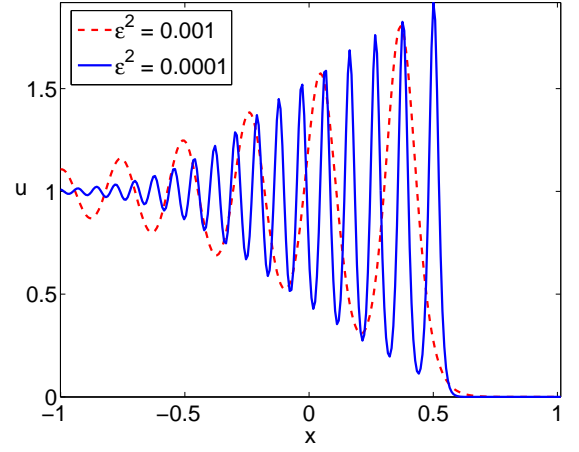


FIG. 8: Numerical solutions of equation (IV.12) for initial data (IV.13) and $\varepsilon^2 = 0.001$ (dashed), $\varepsilon^2 = 0.0001$ (solid). As ε decreases, the wavelength of the oscillations decreases.

\vec{u}_{i-1} , and $\vec{u}_r = \vec{u}_i$. Whereas a shock has just one speed, associated with every rarefaction wave solution $\vec{w}_i(x/t)$ are two speeds v_i^- and v_i^+ .

The established theory of classical shock waves involves dissipative regularizations of conservation laws. For initial step data, the Riemann problem, there are two types of self-similar solutions of interest, a shock wave and a rarefaction wave. In the next section, we study what happens in the region nearby breaking when a dispersive, rather than dissipative, term is used to regularize the conservation law. It will be shown that self-similarity plays a crucial role and that a dispersive shock wave corresponds, in some sense, to a simple rarefaction wave solution of a system of conservation laws.

B. Dispersive Shock Waves, Korteweg-deVries Equation

As a simple model of dispersive shock waves (DSWs) (e.g. in plasmas [18]), we consider the Korteweg-deVries (KdV) equation

$$u_t + \left(\frac{1}{2}u^2\right)_x = -\varepsilon^2 u_{xxx}, \quad (\text{IV.12})$$

for $\varepsilon^2 \ll 1$. We investigate the behavior of the solution to the initial value problem (IVP)

$$u(x, 0; \varepsilon) = \begin{cases} 1 & x \leq 0 \\ 0 & x > 0 \end{cases} \quad (\text{IV.13})$$

as $\varepsilon^2 \rightarrow 0$. This is a Riemann problem in the context of a dispersive regularization of the conservation law (IV.4) with no inherent dissipation.

Figure 8 depicts two numerical solutions to the IVP (IV.12) and (IV.13) for small ε^2 . Oscillations develop about the initial discontinuity with wavelength proportional to ε . Then, as $\varepsilon^2 \rightarrow 0$, an infinite number of

oscillations develop. To understand this behavior, one can employ Whitham's method [19] which is an extension of the Krylov/Bogoliubov method of averaging for ODEs to PDEs. The essence of the technique is to assume that the KdV equation (IV.12) has a uniformly traveling wave solution and average the PDE's conservation laws over fast oscillations allowing certain parameters (such as amplitude, wavelength, and speed) to vary slowly in time and space. Gurevich and Pitaevskii [20] applied Whitham's method to the IVP considered here with boundary matching where one derives boundary conditions for the oscillatory region based on continuity of the averaged flow. We will follow Gurevich and Pitaevskii's work, applying the method of initial data regularization presented in [21] rather than boundary matching to asymptotically solve the initial value problem (IV.12) and (IV.13) in the limit $\varepsilon^2 \rightarrow 0$. This limit, denoted \bar{u} , is a *weak limit* where one averages over the oscillations and is different from the Burgers' shock strong limit depicted in Fig. 7. The Whitham method describes the asymptotic (large t) behavior of the slowly modulated oscillatory region seen in Fig. 8, which is a dispersive shock wave, by enabling an explicit calculation of the weak limit \bar{u} .

Just as a discontinuity represents an idealized dissipative shock wave in a compressible fluid, the weak limit \bar{u} represents an idealized dispersive shock wave. Any compressible gas will have a small but non-zero amount of dissipation. Since a strong limit exists, the transition from small to zero dissipation is smooth. In the case of a DSW, where a weak limit prevails, the transition from small to zero dispersion is accompanied by an infinite number of oscillations. Thus, any physical DSW with small but non-zero dispersion will consist of a finite number of oscillations. However, the weak limit \bar{u} provides an understanding of the physical DSW structure and its associated speeds. As we will show, it also enables clear comparisons between classical and dispersive shock waves.

The first step in the Whitham averaging method is to obtain a quasi-stationary periodic solution. Assuming the traveling wave ansatz, $u(x, t; \varepsilon) = \phi(\theta)$, $\theta = (x - Vt)/\varepsilon$, equation (IV.12) reduces to

$$-V\phi' + \phi\phi' + \phi''' = 0.$$

Integrating this ODE twice we obtain

$$(\phi')^2 = -\frac{1}{3}(\phi^3 - 3V\phi^2 + A\phi + B) \equiv \frac{1}{3}P(\phi),$$

with A and B arbitrary integration constants. Solutions to equations of this form, when $P(\phi)$ is a cubic or quartic polynomial, are elliptic functions. We write the polynomial P in terms of its roots

$$P(\phi) = (\lambda_1 - \phi)(\lambda_2 - \phi)(\lambda_3 - \phi), \quad \lambda_1 \leq \lambda_2 \leq \lambda_3.$$

For convenience, we make the following linear transfor-

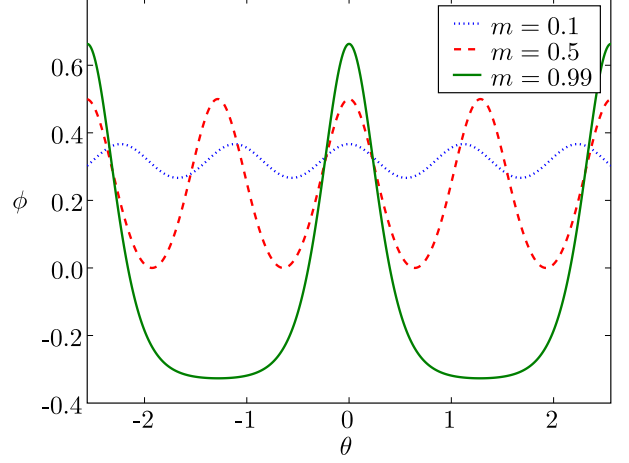


FIG. 9: Elliptic function solutions to the KdV equation for several choices of the parameters $\{r_i\}$. The solution converges to a constant as $m \rightarrow 0$ and to the soliton sech profile as $m \rightarrow 1$.

mation

$$r_1 = \frac{1}{2}(\lambda_1 + \lambda_2), \quad r_2 = \frac{1}{2}(\lambda_1 + \lambda_3), \quad r_3 = \frac{1}{2}(\lambda_2 + \lambda_3), \\ r_1 \leq r_2 \leq r_3.$$

Then the elliptic function solution can be written as (see [22])

$$\phi(\theta) = r_1 + r_2 - r_3 + 2(r_3 - r_1) \operatorname{dn}^2\left(\sqrt{\frac{r_3 - r_1}{6}}\theta; m\right) \\ m = \frac{r_2 - r_1}{r_3 - r_1}, \quad \theta = \frac{x - Vt}{\varepsilon}, \quad V = \frac{1}{3}(r_1 + r_2 + r_3). \quad (\text{IV.14})$$

This is an exact solution to equation (IV.12) with three free parameters $\{r_i\}$ related to the amplitude: $\max(\phi) - \min(\phi) = 2(r_2 - r_1)$, speed V , and wavelength

$$L = 2K(m)\sqrt{\frac{6}{r_3 - r_1}},$$

where $K(m)$ is the complete elliptic integral of the first kind. Note that L is obtained from the periodicity of the dn function (IV.14) i.e. $[\sqrt{\frac{r_3 - r_1}{6}}\theta] = 2K(m)$ where $[\cdot]$ is the period of the argument. The parameter m is the modulus of the elliptic function. See Fig. 9 for a plot of ϕ for various values of m . There are two limiting behaviors $\operatorname{dn}(y; 0) = 1$ and $\operatorname{dn}(y; 1) = \operatorname{sech}(y)$, the solitary wave solution.

The basic idea behind Whitham theory is in the process of averaging over “fast” oscillations. This yields the behavior of the weak limit, \bar{u} , of equation (IV.12) as $\varepsilon \rightarrow 0$. Since ε is assumed to be much smaller than 1 in eq. (IV.12), the phase $\theta = (x - Vt)/\varepsilon$ is a fast

variable. We assume that modulations of this periodic solution take place on the scale of the “slow” variables x and t . Then the average of ϕ is

$$\begin{aligned}\bar{\phi}(x, t) &= \frac{1}{L} \int_0^L \phi(\theta, x, t) d\theta \\ &= r_1(x, t) + r_2(x, t) - r_3(x, t) + \\ &\quad 2[r_3(x, t) - r_1(x, t)] \frac{E[m(x, t)]}{K[m(x, t)]}\end{aligned}\quad (\text{IV.15})$$

where $E(m)$ is the complete elliptic integral of the second kind.

The next step is to write down the first three conservation equations for the KdV equation [23]

$$\begin{aligned}u_t + \left(\frac{1}{2}u^2 + \varepsilon^2 u_{xx}\right)_x &= 0 \\ \left(\frac{1}{2}u^2\right)_t + \left(\frac{1}{3}u^3 + \varepsilon^2 u u_{xx} - \frac{1}{2}\varepsilon^2 u_x^2\right)_x &= 0 \\ \left(\frac{1}{3}u^3 - \varepsilon^2 u_x^2\right)_t + \\ \left(\frac{1}{4}u^4 - 2\varepsilon^4 u_x u_{xxx} + \varepsilon^4 u_{xx}^2 + \varepsilon^2 u^2 u_{xx} - 2\varepsilon^2 u u_x^2\right)_x &= 0.\end{aligned}\quad (\text{IV.16})$$

We require three equations because there are three parameters $\{r_i\}$ that are allowed to slowly vary in time and space. Now we insert the periodic elliptic function solution ϕ into equations (IV.16) and average the equations over the period L to find

$$\begin{aligned}(\bar{\phi})_t + \left(\frac{1}{2}\bar{\phi}^2\right)_x &= 0 \\ \left(\frac{1}{2}\bar{\phi}^2\right)_t + \left(\frac{1}{3}\bar{\phi}^3 - \frac{3}{2}\bar{\phi}_\theta^2\right)_x &= 0 \\ \left(\frac{1}{3}\bar{\phi}^3 - \bar{\phi}_\theta^2\right)_t + \left(\frac{1}{4}\bar{\phi}^4 - 4\bar{\phi}\bar{\phi}_\theta^2 + 3\bar{\phi}_\theta^3\right)_x &= 0.\end{aligned}$$

Note that $\phi_x = \phi_\theta/\varepsilon$.

Assuming that the parameters $\{r_i\}$ depend on the slow variables x and t , the above equations can be transformed to Riemann invariant form [19, 20]

$$\frac{\partial r_i}{\partial t} + v_i(r_1, r_2, r_3) \frac{\partial r_i}{\partial x} = 0, \quad i = 1, 2, 3. \quad (\text{IV.17a})$$

The variables $\{r_i\}$ are the Riemann invariants for the hyperbolic system (IV.17a) with the velocities

$$\begin{aligned}v_1 &= \frac{1}{3}(r_1 + r_2 + r_3) - \frac{2}{3}(r_2 - r_1) \frac{K(m)}{K(m) - E(m)} \\ v_2 &= \frac{1}{3}(r_1 + r_2 + r_3) - \frac{2}{3}(r_2 - r_1) \frac{(1-m)K(m)}{E(m) - (1-m)K(m)} \\ v_3 &= \frac{1}{3}(r_1 + r_2 + r_3) - \frac{2}{3}(r_3 - r_1) \frac{(1-m)K(m)}{E(m)}.\end{aligned}\quad (\text{IV.17b})$$

We wish to solve equations (IV.17) subject to the initial data (IV.13). This is accomplished by the method of initial data regularization, presented in [21]. Although

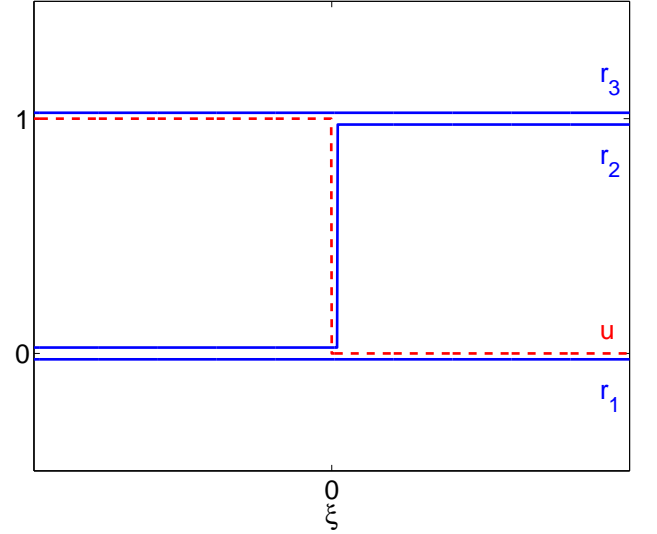


FIG. 10: Initial data regularization for the KdV dispersive Riemann problem. The dashed line represents the initial data (IV.13) for u . The solid lines represent the initial data for the Riemann invariants r_1 , r_2 , and r_3 that regularize the initial data for u . This initial data for the Riemann invariants satisfies the three properties of characterization, non-decreasing, and ordering (IV.19) so a rarefaction wave solution exists for all time (see Fig. 11).

the background to this method involves a detailed understanding of inverse spectral theory and Riemann surface theory, the method itself is straightforward. Any solution to equation (IV.4) with decreasing initial data will eventually break. The dissipative regularization handles this by introducing jump conditions across the shock relating its speed to its values before and after the discontinuity. The dispersive regularization employs the higher order hyperbolic system (IV.17) with initial data that *characterizes* the initial data for u , is *non-decreasing*, and satisfies a *separability* condition. The initial data

$$r_1(x, 0) \equiv 0, \quad r_2(x, 0) = \begin{cases} 0 & x \leq 0 \\ 1 & x > 0 \end{cases}, \quad r_3(x, 0) \equiv 1, \quad (\text{IV.18})$$

shown in Fig. 10 regularizes the IVP (IV.12) and (IV.13) because of the following properties

$$\begin{aligned}\bar{\phi}(x, 0) &= u(x, 0; \varepsilon) && (\text{characterization}), \\ \frac{\partial r_i}{\partial x}(x, 0) &\geq 0 && (\text{non-decreasing}), \\ \max_{x \in \mathbb{R}} r_i(x, 0) &< \min_{x \in \mathbb{R}} r_{i+1}(x, 0) && (\text{separability}).\end{aligned}\quad (\text{IV.19})$$

Characterization amounts to verifying that the initial data for the full problem (IV.13) is equivalent to the initial data for the averaged problem $\bar{\phi}$; the same assumption is made in the boundary matching method [20]. The non-decreasing and separability of the r_i ensure that a global, continuous (non-breaking) solution to the Whitham equations (IV.17) exists for all time [15, 24].

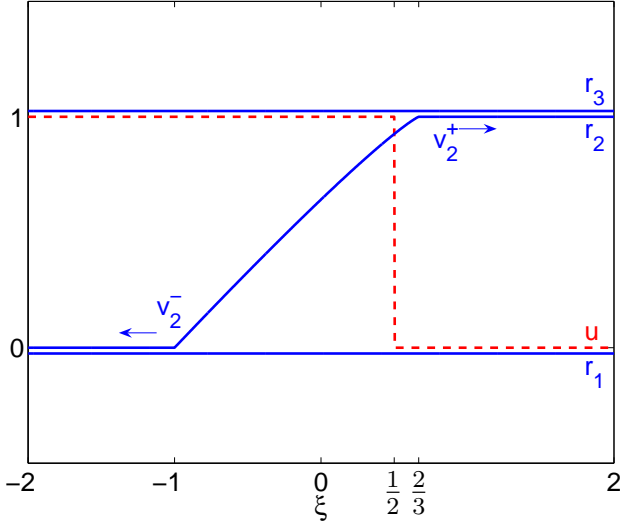


FIG. 11: Dissipative (dashed) and dispersive (solid) regularizations of the conservation law (IV.4). The dissipative case corresponds to a traveling discontinuity with speed $\frac{1}{2}$ satisfying the jump condition (IV.9). The dispersive case is a rarefaction wave solution to the Whitham equations (IV.17) with two associated speeds $v_2^+ = 2/3$ and $v_2^- = -1$. This rarefaction wave modulates the periodic solution (IV.14) giving a DSW (see Fig. 12 and eq. (IV.23)).

The system (IV.17) with initial data (IV.18) has an exact rarefaction solution in the form of a self-similar simple wave with $r_1 \equiv 0$, $r_3 \equiv 1$, and $r_2(x, t) = r_2(\xi)$, $\xi = x/t$. The remaining nontrivial equation in (IV.17a) takes the form

$$(v_2 - \xi)r_2' = 0,$$

which is satisfied when the implicit relation $v_2 = \xi$ or

$$\frac{1}{3}[1 + r_2(\xi)] - \frac{2}{3}r_2(\xi) \frac{[1 - r_2(\xi)]K[r_2(\xi)]}{E[r_2(\xi)] - [1 - r_2(\xi)]K[r_2(\xi)]} = \xi, \quad (\text{IV.20})$$

is satisfied. The above is one equation for one unknown, $r_2(\xi)$, which is solved by a standard root finding method for each ξ (see Fig. 11).

The rarefaction wave has two associated speeds v_2^- and v_2^+ which are determined from the Whitham equations (IV.17). Ahead of the moving fronts, the r_i are constant. Since

$$\frac{dr_2}{dt} = 0, \quad \text{when} \quad \frac{dx}{dt} = v_2,$$

from equations (IV.17b), the speeds are given by the limits

$$v_2^+ = \lim_{r_2 \rightarrow 1^-} v_2(0, r_2, 1) = \frac{2}{3}, \quad (\text{IV.21})$$

$$v_2^- = \lim_{r_2 \rightarrow 0^+} v_2(0, r_2, 1) = -1. \quad (\text{IV.22})$$

The dispersive Riemann problem, equation (IV.12) with initial data (IV.13) or, equivalently, equations

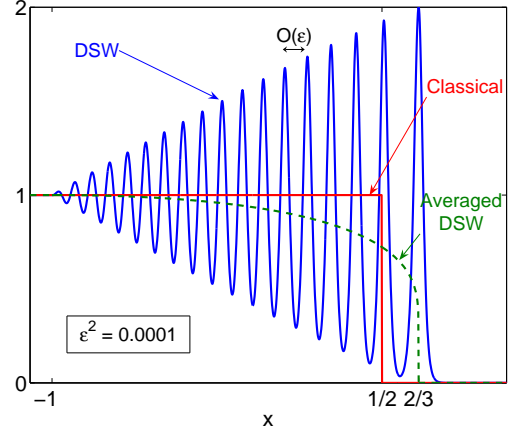


FIG. 12: Comparison of a dispersive shock (eq. (IV.23) with $\varepsilon^2 = 0.0001$), its average $\bar{\phi}$ (eq. (IV.15), dashed), and a classical, dissipative shock (eq. (IV.3), Burgers' solution) plotted at time $t = 1$. The DSW front moves faster than its classical counterpart. The average $\bar{\phi}$ looks very similar to the classical shock, a steep front connected to a constant in the rear, except that the speed of the front is different and the function is continuous.

(IV.14) and (IV.17) with initial data (IV.18), has the asymptotic ($t \gg 1$ and $\varepsilon^2 \ll 1$) DSW solution

$$u(x, t; \varepsilon) \approx r_2(x/t) - 1 + 2\text{dn}^2\left(\frac{x - V(x/t)t}{\varepsilon\sqrt{6}}; m = r_2(x/t)\right) \quad (\text{IV.23})$$

$$V(x/t) = \frac{1}{3}(1 + r_2(x/t)).$$

The function $r_2(x/t)$ is the rarefaction wave solution satisfying equation (IV.20). This DSW solution, its average (eq. (IV.15)), and the Burgers type classical shock solution (IV.3) are shown in Fig. 12. The DSW averaging process produces a shock front that resembles the classical shock front but, however, has a different speed and the DSW front is continuous. The front speed of the DSW, $\frac{2}{3}$, is the phase speed of the classical soliton solution to KdV which fixes an amplitude of 2

$$u(x, t) = 2 \text{sech}^2\left(\frac{1}{\sqrt{6\varepsilon^2}}(x - \frac{2}{3}t)\right).$$

One can think of a DSW as a slowly modulated train of solitons decaying, in a self-similar fashion, to a constant. The DSW is based on the rarefaction solution (IV.20) so it has two associated speeds, the trailing edge v_2^- (IV.22) and the leading edge v_2^+ (IV.21). Even though the DSW is non-zero as $x \rightarrow -\infty$, the oscillations remain in a finite region of space describing the expanding behavior of a steep gradient in this dispersive system.

In Fig. 13, we show the numerical solution to the KdV equation with the step initial data (IV.13) for $\varepsilon^2 = 0.001$. The wavelength of oscillation, leading edge amplitude, and speed of the asymptotic solution agree well with the numerical result. The position of the leading edges differ slightly because the asymptotic solution is valid for $t \gg 1$

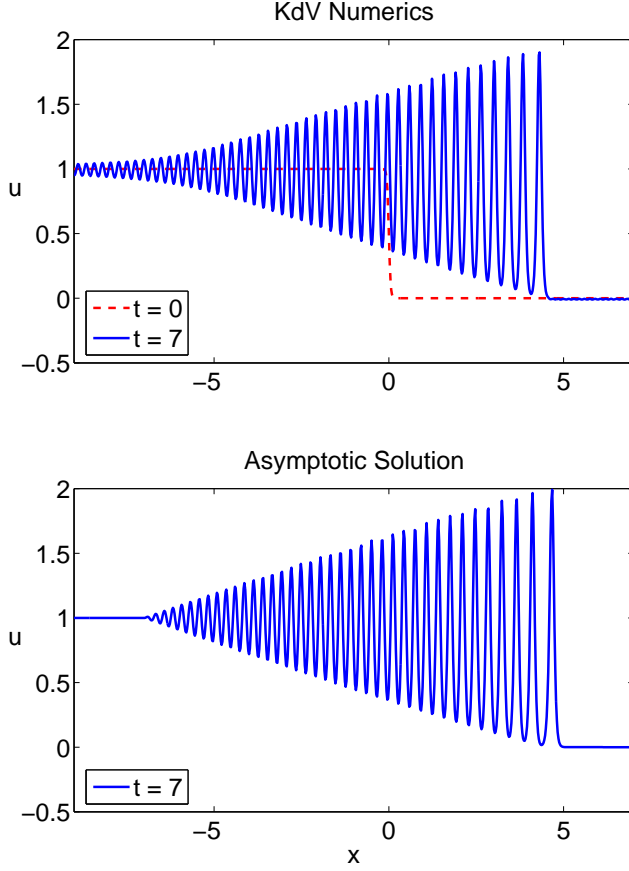


FIG. 13: Numerical solution of the KdV equation with an initial step (top) and the asymptotic DSW solution (IV.23) (bottom) for $\varepsilon^2 = 0.001$.

and it takes the numerical solution some time to reach this stage. Note that the speed of the leading edge in the numerical solution, averaged from $t = 5$ to $t = 7$, is 0.660 which is approximately $\frac{2}{3}$, the analytical result (IV.21).

If the initial data for the KdV equation (IV.12) is non-decreasing then no breaking occurs and a global solution exists for the zero dispersion limit ($\varepsilon^2 \rightarrow 0$). For the case

$$u(x, 0; \varepsilon) = \begin{cases} 0 & x < 0 \\ 1 & x > 0 \end{cases}, \quad (\text{IV.24})$$

the solution is a rarefaction wave, a weak solution satisfying the conservation law (IV.4). This is the Burgers rarefaction wave (IV.8) (see Fig. 14).

Whitham averaging provides an effective way to define the DSW shock speeds and derive the asymptotic oscillatory structure of a DSW along with its leading amplitude. We note that in any experiment ε will be finite hence oscillations will exist. The averaged solution is useful when comparing with gas dynamics since we can evaluate the jump in density across a DSW region and determine the velocity of a DSW shock front.

The long time asymptotic behavior of the KdV equation has been analyzed in [25]. In general, an arbitrary

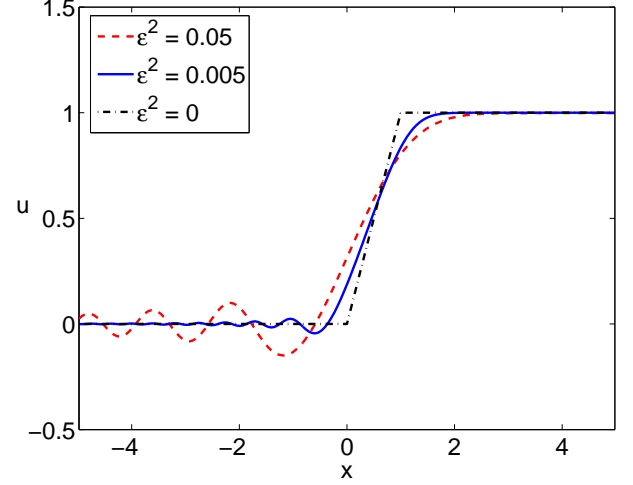


FIG. 14: Numerical solution of the KdV equation (IV.12) with the step initial data (IV.24) for different values of ε and the zero dissipation/dispersion limit $\varepsilon = 0$, the rarefaction wave (IV.8). The plot corresponds to $t = 1$.

initial condition will evolve into a dispersive tail [25], a set of solitons [26, 27], and a "collisionless shock" region [25]. In a sense, the asymptotic solution in Fig. 12 contains all of these regions. The very front of the oscillations is the collisionless shock region over which a constant connects to a train of sech^2 solitons eventually leading to small, linear oscillations at the tail.

Thus we have described how to study a dispersive shock wave associated with KdV in the context of Whitham theory. A DSW can arise in the dispersive regularization of a conservation law just as a classical shock can arise in the dissipative regularization of a conservation law. The key difference is that a *weak limit* where one averages over the oscillations is required in the dispersive case. This method gives useful results such as the asymptotic modulated oscillatory profile, the wavelength of oscillation, the leading amplitude, and the speeds of a dispersive shock. On a large scale, once the limiting process has been accomplished, the DSW and classical shock look similar, i.e. constants connected by sharp gradients. However, the shock speeds are different.

On a small mathematical note, Lax and Levermore [28] used the inverse scattering transform to take the limit $\varepsilon \rightarrow 0$ in the KdV equation (IV.12) for a broad class of initial data. They showed that the limit, \bar{u} , is a weak limit in the sense that

$$\lim_{\varepsilon \rightarrow 0} \int_{-\infty}^{\infty} u(x, t; \varepsilon) f(x) dx = \int_{-\infty}^{\infty} \bar{u}(x, t) f(x) dx$$

for all smooth, compactly defined functions $f(x)$. This type of limiting procedure is required because the solution develops an infinite number of oscillations. Lax and Levermore also showed that, in a region of breaking, the weak limit \bar{u} can be calculated explicitly by using the Whitham averaging method thus giving the method a

strong mathematical footing.

Throughout the rest of this paper, we will use this dissipative/dispersive analogy with the Burgers' and KdV equations to motivate our discussion of the more complicated problem involving the dissipative and dispersive regularizations arising in the context of BEC and gas dynamics.

C. Dissipative Regularization of the Euler Equations

As mentioned in the introduction, the compressible equations of gas dynamics without dissipation are the same as the local conservation equations for a BEC (1.5) with $\varepsilon = 0$. Let us consider the Riemann problem for the dissipative regularization of the Euler equations in one dimension with step initial data

$$\begin{aligned} \rho_t + (\rho u)_x &= 0 \\ (\rho u)_t + (\rho u^2 + \frac{1}{2}\rho^2)_x &= 0 \\ \rho(x, 0) &= \begin{cases} \rho_0 & x < 0 \\ 1 & x > 0 \end{cases}, \quad u(x, 0) = \begin{cases} u_0 & x < 0 \\ 0 & x > 0 \end{cases}. \end{aligned} \quad (\text{IV.25})$$

This is a general step initial value problem with two parameters ρ_0 and u_0 . Note if we make the transformation

$$\begin{aligned} \tilde{\rho} &= \rho_r \rho, \quad \tilde{u} = \sqrt{\rho_r} u + u_r, \\ t &= \rho_r \tilde{t}, \quad x = \sqrt{\rho_r}(\tilde{x} - u_r \tilde{t}), \quad \rho_r \neq 0, \end{aligned} \quad (\text{IV.26})$$

then we convert the initial conditions in (IV.25) to the general step initial conditions

$$\begin{aligned} \tilde{\rho}(\tilde{x}, 0) &= \begin{cases} \rho_l = \rho_r \rho_0 & \tilde{x} < 0 \\ \rho_r & \tilde{x} > 0 \end{cases} \\ \tilde{u}(\tilde{x}, 0) &= \begin{cases} u_l = \sqrt{\rho_r} u_0 + u_r & \tilde{x} < 0 \\ u_r & \tilde{x} > 0 \end{cases}. \end{aligned}$$

The unique weak solution to (IV.25) consists of, in general, three constant states connected to one another via two wave solutions: shocks or centered rarefaction waves (this is a special case of (IV.10) for $n = 2$). We will first study the canonical, right-going shock case which consists of two constant states connected by a traveling discontinuity.

The jump conditions (IV.9) for the IVP (IV.25) are, assuming a traveling wave shock,

$$\begin{aligned} V(\rho_0 - 1) &= \rho_0 u_0 \\ V(\rho_0 u_0) &= \rho_0 u_0^2 + \frac{1}{2}\rho_0^2 - \frac{1}{2}. \end{aligned} \quad (\text{IV.27})$$

A physically realizable shock solution must satisfy an entropy condition, the statement that across any shock wave, there must be a corresponding increase in entropy. For the Riemann problem (IV.25), the entropy condition

for a right going shock is simply $\rho_0 > 1$ [17]. The entropy condition and the jump conditions (IV.27) determine a classical shock wave uniquely. Solving for u_0 and V in (IV.27) gives

$$u_0 = \pm(\rho_0 - 1)\sqrt{\frac{1}{2}(1 + \frac{1}{\rho_0})}, \quad (\text{IV.28})$$

with the corresponding shock speed

$$V = \frac{\rho_0 u_0}{\rho_0 - 1}.$$

For an entropy satisfying right-going shock, we take the plus sign in (IV.28). With this specific choice for u_0 , the Riemann problem (IV.25) has the unique weak solution, parameterized by ρ_0 ,

$$\rho(x/t) = \begin{cases} \rho_0 & x/t < V \\ 1 & x/t > V \end{cases}, \quad u(x/t) = \begin{cases} u_0 & x/t < V \\ 0 & x/t > V \end{cases},$$

a shock moving with speed

$$V = \rho_0 \sqrt{\frac{\rho_0 - 1/\rho_0}{2(\rho_0 - 1)}}.$$

Note that for a right-going shock to exist, there must be a non-zero density ρ on the right. Otherwise, the solution is purely a rarefaction wave [17].

When $\rho_0 < 1$, a pure rarefaction solution exists for the specific choice

$$u_0 = 2(\sqrt{\rho_0} - 1).$$

This choice is a consistency condition for the existence of a continuous rarefaction wave connecting the left constant state $(\rho_0, \rho_0 u_0)$ and the right state $(1, 0)$ [17]. The rarefaction solution is given by (also see Fig. 20)

$$\begin{aligned} \rho(x/t) &= \begin{cases} \rho_0 & x/t < (3\sqrt{\rho_0} - 2) \\ \frac{1}{9}(2 + x/t)^2 & (3\sqrt{\rho_0} - 2) < x/t < 1 \\ 1 & 1 < x/t \end{cases} \\ u(x/t) &= \begin{cases} 2\sqrt{\rho_0} - 2 & x/t < (3\sqrt{\rho_0} - 2) \\ \frac{1}{3}(-2 + 2x/t)^2 & (3\sqrt{\rho_0} - 2) < x/t < 1 \\ 0 & 1 < x/t \end{cases}. \end{aligned} \quad (\text{IV.29})$$

By manipulation, the Euler equations (IV.25) can be written in the Riemann invariant form

$$\begin{aligned} \frac{\partial r_+}{\partial t} + \frac{1}{4}(r_+ + 3r_-)\frac{\partial r_+}{\partial x} &= 0 \\ \frac{\partial r_-}{\partial t} + \frac{1}{4}(3r_+ + r_-)\frac{\partial r_-}{\partial x} &= 0 \\ r_+ &= u + 2\sqrt{\rho}, \quad r_- = u - 2\sqrt{\rho} \end{aligned} \quad (\text{IV.30})$$

These equations yield a general solution of the form (IV.10). In the next section, we will compare the solution of equations (IV.30) to the zero dispersion limit of the GP equation.

The dissipative regularization of the Euler equations—the jump conditions (IV.27)—gives a criterion for determining the speed of a classical shock wave given the initial jump in density. In the next section, we will discuss DSWs in BEC and show that rarefaction waves play a crucial role in their understanding.

D. Dispersive Regularization of the Euler Equations, BEC

Consider equations (I.5), the local conservation equations for a BEC, with $\varepsilon^2 \rightarrow 0$. This is the zero dispersion limit of the GP equation, which we consider as the dispersive regularization of the Euler equations considered in the previous section. Assuming free expansion of the condensate or zero potential, $V = 0$, the GP equation is equivalent to the 3D, defocusing nonlinear Schrödinger equation (NLS). Later we show that the 1D NLS equation gives good qualitative agreement with the three dimensional problem in the so-called “blast wave” regime. In this regard, the Whitham averaging method is a useful device to analyze DSWs in a BEC. It has been used to analyze the 1D defocusing NLS equation in the case of an initial jump in density and velocity using boundary matching [6, 29, 30]. We apply Whitham averaging to the 1D NLS equation using initial data regularization as presented in [21, 31] to derive the shock structure of the canonical 1D BEC DSW along with its associated speeds. This technique is equivalent to the boundary matching method for a single dispersive shock wave. It also allows for generalizations to more complicated, multi-phase type interactions which we will study in the future.

For small dispersion, oscillations begin to develop in breaking regions. As in the KdV case, a strong limit does not exist; hence we are lead to consider a weak limit where one averages over the oscillations. Consider the dispersive Riemann problem for BEC in one dimension without an external potential V , which models a freely expanding condensate

$$\begin{aligned} \rho_t + (\rho u)_x &= 0 \\ (\rho u)_t + (\rho u^2 + \frac{1}{2}\rho^2)_x &= \frac{\varepsilon^2}{4} \left(\rho (\log \rho)_{xx} \right)_x \\ \rho(x, 0; \varepsilon) &= \begin{cases} \rho_0 & x < 0 \\ 1 & x > 0 \end{cases}, \quad u(x, 0; \varepsilon) = \begin{cases} u_0 & x < 0 \\ 0 & x > 0 \end{cases}. \end{aligned} \quad (\text{IV.31})$$

Recall that $\rho = |\Psi|^2$ represents the condensate density and $u = \varepsilon(\arg \Psi)_x$ is the condensate flow velocity. These initial conditions are general step-like data (see (IV.26)).

To apply Whitham theory, we require a periodic solution to equation (IV.31), the local conservation equations for the 1D NLS equation

$$i\varepsilon\Psi_t + \frac{1}{2}\varepsilon^2\Psi_{xx} - |\Psi|^2\Psi = 0. \quad (\text{IV.32})$$

Assume a traveling wave solution of the form

$$\Psi(x, t) = A(\theta)e^{i\phi(\theta)/\varepsilon}, \quad \theta = (x - Vt)/\varepsilon.$$

Inserting this ansatz into equation (IV.32), and equating real and imaginary parts gives

$$\begin{aligned} -VA' + \phi'A' + \frac{1}{2}\phi''A &= 0 \\ V\phi'A + \frac{1}{2}A'' - \frac{1}{2}\phi'^2A - A^3 &= 0. \end{aligned} \quad (\text{IV.33})$$

Integrating the first equation and solving for ϕ' , we find

$$\phi' = V - \frac{2c_1}{A^2},$$

where c_1 is a constant of integration. Inserting this result into the second equation in (IV.33) and simplifying gives

$$A'' + V^2A - \frac{4c_1^2}{A^3} - 2A^3 = 0.$$

Integrating this equation gives

$$A'^2 + V^2A^2 + \frac{4c_1^2}{A^2} - A^4 + c_2 = 0, \quad (\text{IV.34})$$

where c_2 is a second constant of integration. To obtain the elliptic function solution, let $\rho = A^2$; then equation (IV.34) becomes

$$\begin{aligned} \rho'^2 &= 4(\rho^3 - V^2\rho^2 - 2c_2\rho - 4c_1^2) \\ &= 4(\rho - \lambda_1)(\rho - \lambda_2)(\rho - \lambda_3), \\ 0 &< \lambda_1 < \lambda_2 < \lambda_3. \end{aligned} \quad (\text{IV.35})$$

The periodic solution to the above equation is [22]

$$\begin{aligned} \rho(x, t) &= \lambda_3 - (\lambda_3 - \lambda_1)\text{dn}^2\left(\sqrt{\lambda_3 - \lambda_1}\frac{(x - Vt)}{\varepsilon}; m\right) \\ u(x, t) &= \phi'(\theta) = V - \frac{2c_1}{\rho(x, t)}, \quad V = \sqrt{\lambda_1 + \lambda_2 + \lambda_3} \\ m &= \frac{\lambda_2 - \lambda_1}{\lambda_3 - \lambda_1}, \quad c_1^2 = \frac{1}{4}\lambda_1\lambda_2\lambda_3. \end{aligned} \quad (\text{IV.36})$$

Similar to the KdV equation, this solution has three independent constants of integration λ_i , $i = 1, 2, 3$, the roots of the cubic polynomial in (IV.35). However, by the invariance of the NLS equation with respect to the “Galilean boost”

$$\Psi(x, t) \rightarrow e^{-i\tilde{V}(x - \frac{1}{2}\tilde{V}t)}\Psi(x - \tilde{V}t, t),$$

the phase speed \tilde{V} is another arbitrary constant. Then the periodic solution to equation (IV.31) is

$$\begin{aligned} \rho(x, t; \varepsilon) &\equiv \psi(\theta) = \lambda_3 - (\lambda_3 - \lambda_1)\text{dn}^2(\sqrt{\lambda_3 - \lambda_1}\theta; m) \\ u(x, t; \varepsilon) &\equiv \nu(\theta) = V - \sigma \frac{\sqrt{\lambda_1\lambda_2\lambda_3}}{\psi(\theta)} \\ m &= \frac{\lambda_2 - \lambda_1}{\lambda_3 - \lambda_1}, \quad \sigma = \pm 1, \quad \theta = \frac{x - Vt}{\varepsilon}, \end{aligned} \quad (\text{IV.37})$$

with four arbitrary parameters V and λ_i , $i = 1, 2, 3$. The sign of the constant of integration c_1 in (IV.36) is not determined. Either sign $\sigma = \pm 1$ gives a valid periodic solution to the NLS equation (IV.32). This will be important later in our analysis of DSWs with points of zero density.

Using Whitham's averaging method, we will derive equations describing slow modulations of the four parameters in the periodic solution (IV.37). Anticipating the form of the Whitham equations, we will express the four aforementioned parameters in terms of four parameters r_i [29]

$$\begin{aligned} V &= \frac{1}{4}(r_1 + r_2 + r_3 + r_4), \\ \lambda_3 &= \frac{1}{16}(-r_1 - r_2 + r_3 + r_4)^2, \\ \lambda_2 &= \frac{1}{16}(-r_1 + r_2 - r_3 + r_4)^2, \\ \lambda_1 &= \frac{1}{16}(r_1 - r_2 - r_3 + r_4)^2, \\ r_1 &< r_2 < r_3 < r_4. \end{aligned} \quad (\text{IV.38})$$

Similar to the KdV system, the parameters r_i correspond to Riemann invariants for the NLS Whitham equations, which we derive now.

The period of the dn function in (IV.37) is $[\sqrt{\lambda_3 - \lambda_1}\theta] = 2K(m)$ where $[\cdot]$ denotes the period of the argument. Then the wavelength of oscillation for the periodic solution (IV.37) is

$$L = \frac{2K(m)}{\sqrt{\lambda_3 - \lambda_1}}. \quad (\text{IV.39})$$

The average of the periodic solution (IV.37) over the wavelength L is [22]

$$\begin{aligned} \overline{\psi}(x, t) &= \frac{1}{L} \int_0^L \psi(\theta) d\theta \\ &= \lambda_3 - (\lambda_3 - \lambda_1) \frac{E(m)}{K(m)} \\ \overline{\psi\nu}(x, t) &= \frac{1}{L} \int_0^L \psi(\theta) \nu(\theta) d\theta \\ &= V\overline{\psi} - \sigma\sqrt{\lambda_1\lambda_2\lambda_3}, \\ \overline{\nu}(x, t) &= \frac{1}{L} \int_0^L \nu(\theta) d\theta \\ &= V - \sigma\sqrt{\frac{\lambda_1\lambda_2}{\lambda_3}} - \sigma\sqrt{\lambda_3 - \lambda_1} \{E(\chi, 1-m) + \\ &\quad F(\chi, 1-m)[E(m)/K(m) - 1]\} \\ \chi &= \sin^{-1}\left(\sqrt{\frac{\lambda_3 - \lambda_1}{\lambda_3}}\right) \end{aligned} \quad (\text{IV.40})$$

The functions $F(\chi, 1-m)$ and $E(\chi, 1-m)$ are incomplete elliptic integrals of the first and second kind respectively [22].

Four conservation laws for the NLS equation are [10, 32]

$$\begin{aligned} \rho_t + (\rho u)_x &= 0 \\ (\rho u)_t + \left(\rho u^2 + \frac{1}{2}\rho^2 - \frac{\varepsilon^2}{4}\rho(\log \rho)_{xx}\right)_x &= 0 \\ \left(\rho u^2 + \rho^2 + \varepsilon^2 \frac{\rho_x^2}{4\rho}\right)_t + \left(\rho u^3 + 2\rho^2 u + \varepsilon^2 \frac{\rho_x^2 u}{4\rho}\right)_x &= 0 \\ \left(\varepsilon^3 \rho_{xxx} - \frac{3}{2}\varepsilon^3 \frac{\rho_x \rho_{xx}}{\rho} + \frac{3}{4}\varepsilon^3 \frac{\rho_x^3}{\rho^2} - 5\varepsilon \rho \rho_x - 3\varepsilon \rho_x u^2 + \right. \\ &\quad \left. 3\varepsilon \rho u u_x\right)_t + \left(\frac{1}{2}\varepsilon^4 \rho_{xxxx} - \frac{5}{4}\varepsilon^4 \frac{\rho_{xxx} \rho_x}{\rho} - \frac{3}{4}\varepsilon^2 \frac{\rho_{xx}}{\rho} + \right. \\ &\quad \left. \frac{21}{8}\varepsilon^4 \frac{\rho_{xx} \rho_x^2}{\rho^2} - \frac{7}{2}\varepsilon^2 \rho \rho_{xx} - \frac{9}{2}\varepsilon^2 u^2 \rho_{xx} - \frac{9}{8}\varepsilon^4 \frac{\rho_x^4}{\rho^3} - \frac{1}{4}\varepsilon^2 \rho_x^2 + \right. \\ &\quad \left. 3\varepsilon^2 \frac{u^2 \rho_x^2}{\rho} - 6\varepsilon^2 u u_x \rho_x + 2\rho^3 + 7\rho^2 u^2 - \right. \\ &\quad \left. 5\varepsilon^2 \rho u u_{xx} - 3\varepsilon^2 \rho u_x^2 + 2\rho u^4 + 2\rho^2 u^2\right)_x = 0 \end{aligned} \quad (\text{IV.41})$$

To obtain the Whitham equations for the $\{r_i\}$, we insert the periodic solution (IV.37) into the conservation laws (IV.41) and average over the fast variable θ to find

$$\begin{aligned} (\overline{\psi})_t + (\overline{\psi\nu})_x &= 0 \\ (\overline{\psi\nu})_t + \left(\overline{\psi\nu^2} + \frac{1}{2}\overline{\psi^2} - \frac{1}{4}\overline{\psi(\log \psi)_{\theta\theta}}\right)_x &= 0 \\ \left(\overline{\psi\nu^2} + \overline{\psi^2} + \frac{\overline{\psi_\theta^2}}{4\psi}\right)_t + \left(\overline{\psi\nu^3} + 2\overline{\psi^2\nu} + \frac{\overline{\psi_\theta^2\nu}}{4\psi}\right)_x &= 0 \\ \left(\frac{3}{4}\frac{\overline{\psi_\theta^3}}{\psi^2} - \frac{3}{2}\frac{\overline{\psi_\theta\psi_{\theta\theta}}}{\psi} - \frac{9}{2}\frac{\overline{\psi_\theta\nu^2}}{\psi}\right)_t + \left(-\frac{5}{4}\frac{\overline{\psi_{\theta\theta\theta}\psi_\theta}}{\psi} - \frac{3}{4}\frac{\overline{\psi_{\theta\theta}}}{\psi} + \right. \\ &\quad \left. \frac{21}{8}\frac{\overline{\psi_{\theta\theta}\psi_\theta^2}}{\psi^2} - \frac{7}{2}\overline{\psi\psi_{\theta\theta}} - \frac{9}{2}\overline{\nu^2\psi_{\theta\theta}} - \frac{9}{8}\frac{\overline{\psi_\theta^4}}{\psi^3} - \frac{1}{4}\overline{\psi_\theta^2} + 3\frac{\overline{\nu^2\psi_\theta^2}}{\psi} + \right. \\ &\quad \left. 2\overline{\psi^3} + 7\overline{\psi^2\nu^2} + \overline{\psi\nu\nu_{\theta\theta}} + 3\overline{\psi\nu_\theta^2} + 2\overline{\psi\nu^4} + 2\overline{\psi^2\nu^2}\right)_x = 0 \end{aligned} \quad (\text{IV.42})$$

Assuming that the four parameters r_i vary on the slow length and time scales x and t , the Whitham equations are obtained [29, 33]

$$\frac{\partial r_i}{\partial t} + v_i(r_1, r_2, r_3, r_4) \frac{\partial r_i}{\partial x} = 0, \quad i = 1, 2, 3, 4. \quad (\text{IV.43a})$$

The v_i are expressions involving complete first and sec-

and elliptic integrals

$$\begin{aligned}
v_1 &= V - \frac{1}{2}(r_2 - r_1) \left[1 - \frac{(r_4 - r_2)E(m)}{(r_4 - r_1)K(m)} \right]^{-1} \\
v_2 &= V + \frac{1}{2}(r_2 - r_1) \left[1 - \frac{(r_3 - r_1)E(m)}{(r_3 - r_2)K(m)} \right]^{-1} \\
v_3 &= V - \frac{1}{2}(r_4 - r_3) \left[1 - \frac{(r_4 - r_2)E(m)}{(r_3 - r_2)K(m)} \right]^{-1} \\
v_4 &= V + \frac{1}{2}(r_4 - r_3) \left[1 - \frac{(r_3 - r_1)E(m)}{(r_4 - r_1)K(m)} \right]^{-1} \\
m &= \frac{(r_4 - r_3)(r_2 - r_1)}{(r_4 - r_2)(r_3 - r_1)}.
\end{aligned} \tag{IV.43b}$$

Thus (the complicated looking) equations (IV.42) reduce to the simple system of first order PDE (IV.43). This reduction takes advantage of certain integrable properties of the NLS equation which we will not discuss here. For further details, the reader is referred to [34].

As in the KdV case, it turns out that the right going dispersive shock wave is characterized by a self-similar, simple rarefaction wave in the associated Whitham equations (IV.43). There are two free parameters in the IVP (IV.31), the initial velocity u_0 and the initial density ρ_0 . As we are seeking a simple wave solution, we require one of the Riemann invariants from the Euler system (IV.30), r_- in this case, to be constant initially. For the initial data in (IV.31), this corresponds to the specific choice for the initial velocity $u_0 = 2(\sqrt{\rho_0} - 1)$ and the initial data

$$r_+(x, 0) = \begin{cases} 4\sqrt{\rho_0} - 2 & x < 0 \\ 2 & x > 0 \end{cases}, \quad r_-(x, 0) \equiv -2. \tag{IV.44}$$

Equations (IV.30) accurately describe a regular solution, hence a dispersive or dissipative regularization of the Euler equations whenever both r_+ and r_- are non-decreasing [21]. A weak limit is not required because a rarefaction type solution exists for all time. In other words, the dissipative and dispersive regularizations are equivalent when no shocks develop.

On the other hand, when the initial data for the Riemann invariants are decreasing, as in the case of (IV.44) with $\rho_0 > 1$, a shock wave will develop.

We now use the technique of initial data regularization [21] where the r_i are chosen initially (see Fig. 15) so that

$$\begin{aligned}
\bar{\psi}(x, 0) &= \rho(x, 0; \varepsilon), \quad \bar{v}(x, 0) = u(x, 0; \varepsilon) \quad (\text{characterization}), \\
\frac{\partial r_i}{\partial x}(x, 0) &\geq 0 \quad (\text{non-decreasing}), \\
\max_{x \in \mathbb{R}} r_i(x, 0) &< \min_{x \in \mathbb{R}} r_{i+1}(x, 0) \quad (\text{separability}).
\end{aligned} \tag{IV.45}$$

Recall that the characterization property implies that the initial data for the full problem and the averaged problem

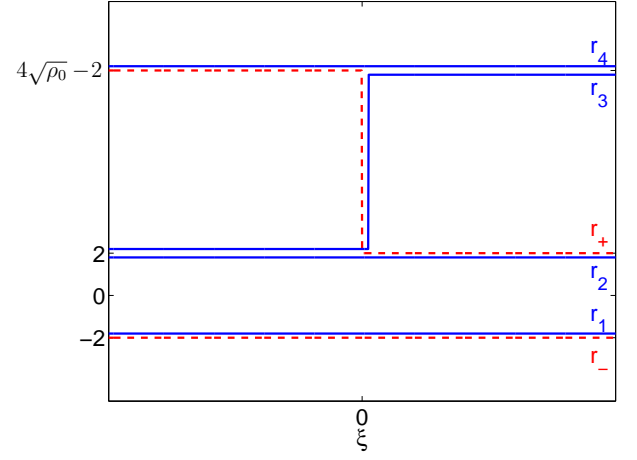


FIG. 15: Regularized initial data for the dispersive Riemann problem (IV.31). The variables r_+ and r_- are the Riemann invariants for the Euler equations satisfying (IV.30). The $\{r_i\}$ are the Riemann invariants for the Whitham equations (IV.43) describing the modulation of a periodic wave (IV.37). The $\{r_i\}$ satisfy the properties of being non-decreasing and separable (IV.45), so a continuous rarefaction solution exists for all time (see Fig. 16).

are the same. For this to be so, we take

$$\begin{aligned}
r_1(x, 0) &\equiv -2, \quad r_2(x, 0) \equiv 2, \quad r_4(x, 0) \equiv 4\sqrt{\rho_0} - 2, \\
r_3(x, 0) &= \begin{cases} 2 & x < 0 \\ 4\sqrt{\rho_0} - 2 & x > 0 \end{cases}.
\end{aligned} \tag{IV.46}$$

We also require a spatial dependence of the sign σ in (IV.40) when $\rho_0 \geq 4$

$$\sigma(x, 0) = \text{sgn}(x) = \begin{cases} -1 & x < 0 \\ 1 & x > 0 \end{cases}. \tag{IV.47}$$

When $1 \leq \rho_0 < 4$, $\sigma \equiv 1$. The non-decreasing and separability properties guarantee that a continuous solution for the hyperbolic system (IV.43) exists for all time [15, 21]. Thus we have regularized the “shock” initial data.

Using the initial data regularization shown in Fig. 15, we solve equations (IV.43) for a self-similar ($\xi = x/t$), simple rarefaction wave. Assuming $r_1 = -2$, $r_2 = 2$, $r_3(x, t) = r_3(\xi)$, and $r_4 = 4\sqrt{\rho_0} - 2$, we find that all the Whitham equations are satisfied if

$$(v_3 - \xi)r_3' = 0.$$

This equation is satisfied for non-constant r_3 when $v_3 =$

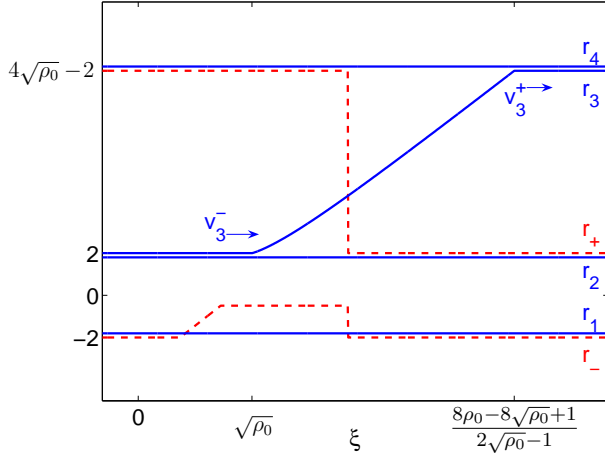


FIG. 16: Solution to classical (dashed) and dispersive (solid) Riemann problems for the Euler equations with initial data shown in Fig. 15. The classical solution consists of three constant states connected by a rarefaction wave and a shock wave. The dispersive regularization involves a pure rarefaction solution of the Whitham equations (IV.43) where only r_3 varies according to (IV.48). This solution modulates the periodic solution (IV.37) giving a DSW (see Fig. 17).

ξ , or explicitly

$$\begin{aligned} \xi &= \frac{1}{4}r_3(\xi) + \sqrt{\rho_0} - \frac{1}{2} - [4\sqrt{\rho_0} - 2 - r_3(\xi)] \times \\ &\quad \times \left[2 - \frac{(8\sqrt{\rho_0} - 8)E(m(\xi))}{(r_3(\xi) - 2)K(m(\xi))} \right]^{-1} \\ m(\xi) &= \frac{4\sqrt{\rho_0} - 2 - r_3(\xi)}{(\sqrt{\rho_0} - 1)(r_3(\xi) + 2)}. \end{aligned} \quad (\text{IV.48})$$

The above is one nonlinear equation for the unknown $r_3(\xi)$. We use a standard root finding method to solve this system. The rarefaction solution for r_3 is shown in Fig. 16 along with the dissipative regularization of the Euler equations (IV.30) for the same initial data. Recall that the general solution for the dissipative Riemann problem has the form (IV.10) for $n = 2$. For the initial data in (IV.44), we find that this general solution consists of three constant states, the first two connected by a rarefaction wave, the latter two connected by a dissipative shock wave (see the dashed curve in Fig. 16).

Inserting the self-similar solution of the Whitham equations (IV.48) into the original periodic solution (IV.37) for the case $1 \leq \rho_0 < 4$ (recall $\sigma \equiv 1$), gives a slowly modulated periodic wave (see Fig. 17), a DSW in BEC.

The speeds of the trailing and leading edges of the DSW are found in the same manner as they were in the

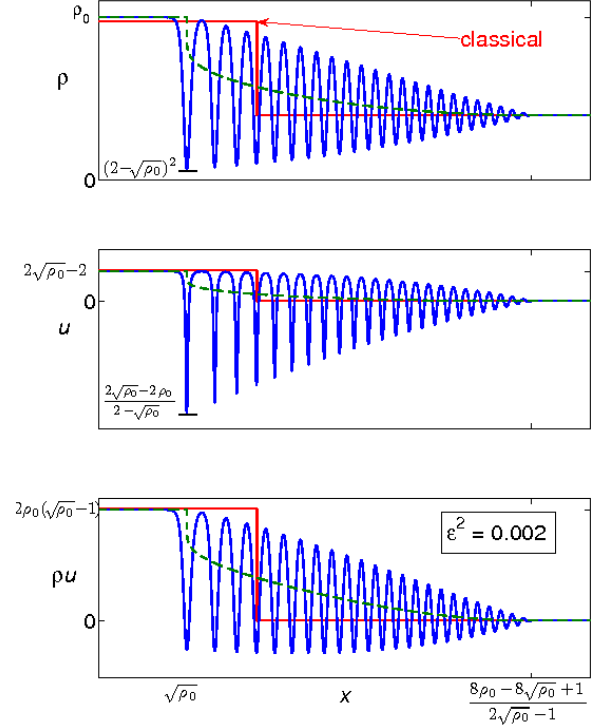


FIG. 17: DSW (GP, oscillatory) and classical shock (Euler, discontinuity). The dashed curve is the averaged DSW. The upper plot is the density ρ , the middle plot is the velocity u , and the lower plot is the momentum ρu for the parameters $\rho_0 = 2.5$, $t = 1$, and $\varepsilon^2 = 0.002$. A DSW in BEC is an expanding region with the constant trailing and leading edge speeds $v_3^- = \sqrt{\rho_0}$ and $v_3^+ = \frac{8\rho_0 - 8\sqrt{\rho_0} + 1}{2\sqrt{\rho_0} - 1}$ respectively. When $1 < \rho_0 < 4$, the DSW looks similar to the one pictured here. For $\rho_0 \geq 4$, the situation is different see Fig. 21. The maximums and minimums of the density and velocity are marked for comparison with the NLS gray soliton solution (IV.50).

KdV case, using equations (IV.43b)

$$\begin{aligned} v_3^- &= \lim_{r_3 \rightarrow 2^+} v_3(-2, 2, r_3, 4\sqrt{\rho_0} - 2) = \sqrt{\rho_0}, \\ v_3^+ &= \lim_{r_3 \rightarrow 4\sqrt{\rho_0} - 2^-} v_3(-2, 2, r_3, 4\sqrt{\rho_0} - 2) \\ &= \frac{8\rho_0 - 8\sqrt{\rho_0} + 1}{2\sqrt{\rho_0} - 1}. \end{aligned} \quad (\text{IV.49})$$

Because the trailing edge speed is the speed of sound (linear disturbances of the Euler equations (IV.25)) in gas dynamics (see e.g. [17]), it might appear that the trailing edge of a DSW is not affected by the nonlinearities in the problem. However a closer examination reveals that the trailing edge speed is exactly the phase speed of a gray soliton with the trailing dip shape given in Fig. 17. A general gray soliton solution to the 1D NLS equation

(IV.32) is

$$\begin{aligned}\Psi(x, t) &= B e^{-i[(B^2 + \frac{1}{2}W^2)t + Wx]/\varepsilon} [\beta \tanh(\theta) + i\mu], \\ \rho &= |\Psi(x, t)|^2 = B^2 [\beta^2 \tanh^2(\theta) + \mu^2], \\ u &= \varepsilon [\arg \Psi(x, t)]_x = -W - \frac{\mu B \beta^2 \operatorname{sech}^2(\theta)}{B^2 \tanh^2(\theta) + \mu^2} \\ \theta &= B\beta[x - (B\mu - W)t - x_0]/\varepsilon.\end{aligned}\quad (\text{IV.50})$$

where all parameters are real and $\mu^2 + \beta^2 = 1$ (see Fig. 18). The speed of the gray soliton is

$$v_g = B\mu - W. \quad (\text{IV.51})$$

It's minimum density and velocity occur when $x = (B\mu - W)t + x_0$ giving the maximum and minimum values

$$\begin{aligned}\rho_{\max} &= \max |\Psi|^2 = B^2, \quad \rho_{\min} = \min |\Psi|^2 = (B\mu)^2, \\ u_{\max} &= \max \varepsilon(\arg \Psi)_x = -W, \\ u_{\min} &= \min \varepsilon(\arg \Psi)_x = B(\mu - \frac{1}{\mu}) - W.\end{aligned}\quad (\text{IV.52})$$

To find the parameters B , μ , and W we relate the maximums and minimums of the general gray soliton in (IV.52) to the maximums and minimums of the trailing dip in the DSW of Fig. 17. Equating maxes and mins for the densities, we find

$$B = \sqrt{\rho_0}, \quad \mu = \frac{2 - \sqrt{\rho_0}}{\sqrt{\rho_0}}. \quad (\text{IV.53})$$

Setting the maximum velocity equal, $-W = 2\sqrt{\rho_0} - 2$, we find

$$W = 2 - 2\sqrt{\rho_0}. \quad (\text{IV.54})$$

So the phase speed (IV.51) of the gray soliton with the parameters (IV.53) and (IV.54) is

$$v_g = \sqrt{\rho_0},$$

equivalent to (IV.49), the DSW trailing edge speed. The trailing edge of the DSW moves with the phase speed of a gray soliton which, in this case, is the sound speed. Therefore, similar to the KdV case and, as argued in [6], the trailing edge of the DSW can be thought of as a modulated train of gray solitons.

In Fig. 19, the asymptotic result depicted in Fig. 17 is compared with direct numerical simulation of the NLS equation with step initial data showing excellent agreement.

The shock profile in Fig. 17 is valid when $1 < \rho_0 < 4$. When $\rho_0 < 1$, the initial data for the Riemann invariants r_+ and r_- (IV.44) is non-decreasing therefore no initial data regularization is required and a rarefaction wave solution exists, see eq. (IV.29) and Fig. 20. The rarefaction solution for the dispersive and dissipative regularizations is the same.

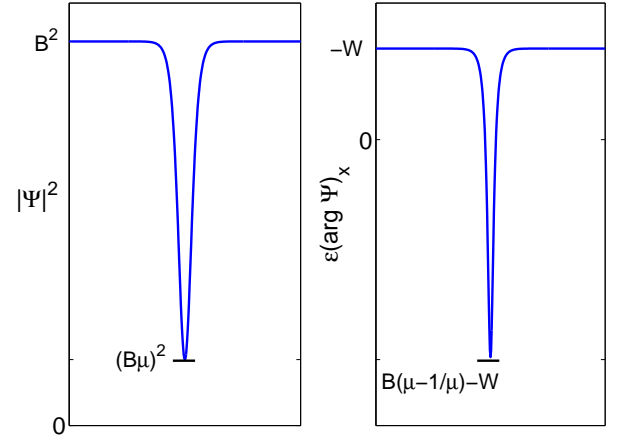


FIG. 18: The density and velocity of the gray soliton solution (IV.50) with labeled maximum and minimum values for comparison with the trailing dip in the DSW Fig. 17.

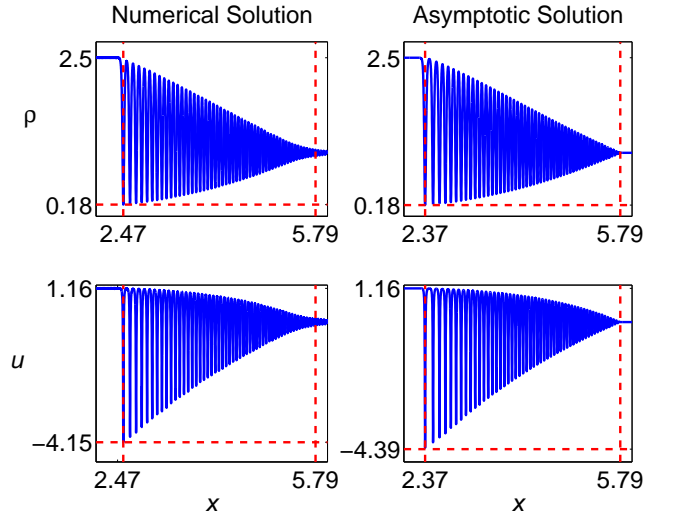


FIG. 19: Numerical solution of the dispersive Riemann problem (left) and its asymptotic solution (right) at $t = 1.5$ for $\rho_0 = 2.5$ and $\varepsilon = 0.03$. The numerically determined trailing edge speed, calculated from $t = 1.2$ to $t = 1.5$, is 1.590, approximately equal to $\sqrt{\rho_0} = 1.581$, the theoretical result (IV.49). The trailing edge density is 0.175, approximately the theoretical value $(2 - \sqrt{\rho_0})^2 = 0.184$.

For the case $\rho_0 \geq 4$, a point of the solution with zero density, a vacuum point, is generated [30]. We label the location of the vacuum point with the similarity variable ξ_v . The minimum density of $\rho(x, t)$ in (IV.37) is $\rho_{\min} = \lambda_1$ (since $\min(-\operatorname{dn}(x)^2) = -\operatorname{dn}(0)^2 = -1$). Solving $\rho_{\min} = \lambda_1 = 0$ at a vacuum point with the constants in (IV.46) ($r_1 = -2$, $r_2 = 2$, $r_4 = 4\sqrt{\rho_0} - 2$) and using equation (IV.38) ($r_1 - r_2 - r_3 + r_4 = 0$) gives $r_3(\xi_v) = 4\sqrt{\rho_0} - 6$. Using the relation (IV.48), the loca-

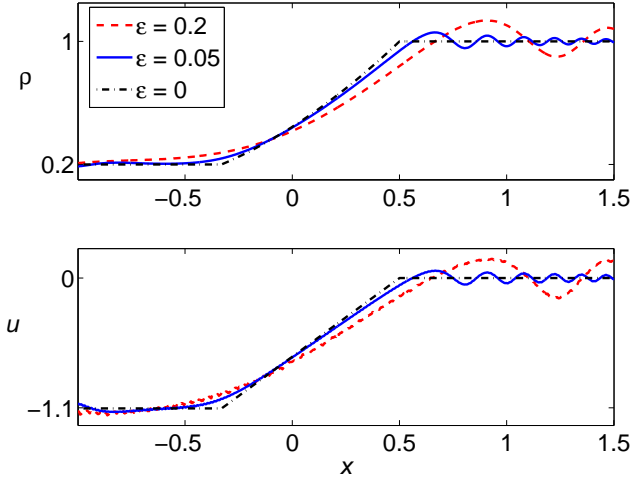


FIG. 20: Numerical solution of the dispersive Riemann problem for rarefaction initial data. As $\varepsilon \rightarrow 0$, the dispersive regularization converges strongly to the dissipative regularization, the rarefaction wave eq. (IV.29). The parameters are $\rho_0 = 0.2$, $u_0 = 2\sqrt{\rho_0} - 2$, and $t = 0.5$.

tion is

$$\xi_v = 2\sqrt{\rho_0} - 2 - 2 \left[1 - \frac{(\sqrt{\rho_0} - 1)E(m_v)}{(\sqrt{\rho_0} - 2)K(m_v)} \right]^{-1} \quad (\text{IV.55})$$

$$m_v = (\sqrt{\rho_0} - 1)^{-2}.$$

When $\rho_0 \geq 4$, the characterization of the initial data in (IV.45) requires that the sign σ in (IV.37) change at the origin (IV.47). Since the modulated periodic solution (IV.37) and its average (IV.40) depend on σ , we must determine how σ depends on x and t . It is natural to assume that the globally conserved momentum $\rho u = i\frac{\varepsilon}{2}(\Psi\Psi_x^* - \Psi^*\Psi_x)$ is smooth. The modulated periodic wave for the momentum is (recall (IV.37))

$$\rho u = V\rho - \sigma\sqrt{\lambda_1\lambda_2\lambda_3}.$$

Since V and ρ are smooth, we consider

$$\sigma\sqrt{\lambda_1\lambda_2\lambda_3} = \frac{1}{64}\sigma|4\sqrt{\rho_0} - 6 - r_3(\xi)| \times (4\sqrt{\rho_0} - 2 - r_3(\xi))(4\sqrt{\rho_0} - 6 + r_3(\xi)).$$

The above expression is derived from the rarefaction solution (IV.48) and the relations (IV.38). Then, for $\sigma\sqrt{\lambda_1\lambda_2\lambda_3}$ to be smooth, we require

$$\sigma(\xi) = \text{sgn}(4\sqrt{\rho_0} - 6 - r_3(\xi)).$$

Since

$$r_3(\xi_v) = 4\sqrt{\rho_0} - 6,$$

the sign change occurs exactly at the vacuum point $\xi = \xi_v$ (IV.55). Thus, σ has the self-similar dependence

$$\sigma(x, t) = \sigma(x/t) = \text{sgn}(x/t - \xi_v) = \begin{cases} -1 & x/t < \xi_v \\ 1 & x/t > \xi_v \end{cases}. \quad (\text{IV.56})$$

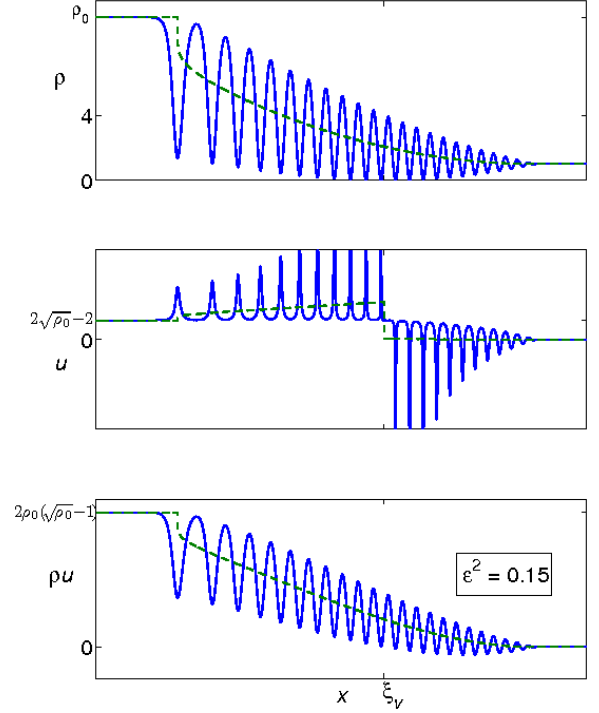


FIG. 21: DSW shock profile (solid) and its average (dashed) plotted at $t = 1$ when $\rho_0 \geq 4$ (here $\rho_0 = 10$) giving rise to a vacuum point at $x/t = \xi_v \approx 7.4$ (see eq. (IV.55)) of zero density and infinite velocity. The average velocity \bar{v} exhibits a jump at the vacuum point but the average momentum $\bar{\rho v}$ does not. This indicates that the variables ρ and ρu are the most natural variables for the problem.

An example DSW profile and its average with a vacuum point at $x/t = \xi_v$, are shown in Fig. 21. At the vacuum point there is a jump in the average velocity \bar{v} . However, there is no jump in the average momentum $\bar{\rho v}$.

For comparison, Fig. 22 is a plot of the average momentum $\bar{\rho v}$ (eq. (IV.40)) and the modulated DSW momentum ψv (eq. (IV.37)) with the *incorrect* choice $\sigma(x, t) \equiv +1$. The trailing edge condition

$$\lim_{x \rightarrow -\infty} \bar{\rho v} = 2\rho_0(\sqrt{\rho_0} - 1) \quad (\text{IV.57})$$

is *not* satisfied. Also, the average momentum is not smooth at the vacuum point $x/t = \xi_v$.

From the plot of the velocity u in Fig. 21, we will argue in the next section that vacuum points appear in the blast wave experiments considered.

In summary, the asymptotic solution for a DSW in a one-dimensional BEC is a slowly modulated periodic

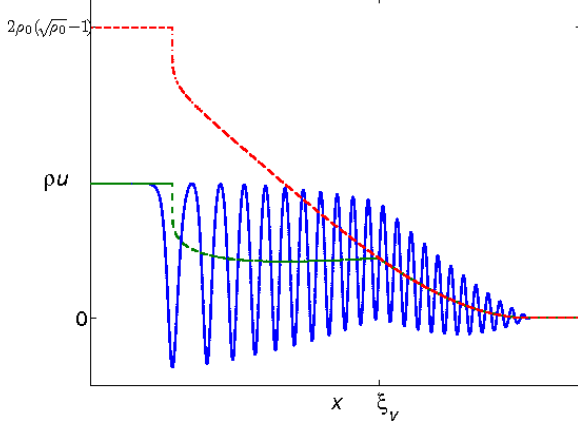


FIG. 22: Average momentum $\overline{\psi\nu}$ (IV.40) (dashed) and the modulated DSW momentum $\psi\nu$ (IV.37) (solid) with the rarefaction solution (IV.48) and the *incorrect* choice of constant sign $\sigma \equiv +1$ and the *correct* choice $\sigma = \text{sgn}(\xi - \xi_v)$ (dash dotted) for $\rho_0 = 10$. The boundary condition (IV.57) is not satisfied and there is a kink at the vacuum point for the incorrect σ .

wave expressed as

$$\begin{aligned}
 \rho(x, t; \varepsilon) &\approx \lambda_3(x/t) - [\lambda_3(x/t) - \lambda_1(x/t)] \times \\
 &\quad \times \text{dn}^2[\sqrt{\lambda_3(x/t) - \lambda_1(x/t)}\theta; m(x/t)], \\
 u(x, t; \varepsilon) &\approx V(x/t) - \sigma(x/t) \frac{\sqrt{\lambda_1(x/t)\lambda_2(x/t)\lambda_3(x/t)}}{\rho(x, t; \varepsilon)}, \\
 m(x/t) &= \frac{\lambda_2(x/t) - \lambda_1(x/t)}{\lambda_3(x/t) - \lambda_1(x/t)}, \\
 V(x/t) &= \frac{1}{4}[4\sqrt{\rho_0} - 2 + r_3(x/t)], \quad \theta = \frac{x - V(x/t)t}{\varepsilon}, \\
 \lambda_1(x/t) &= \frac{1}{16}[4\sqrt{\rho_0} - 6 - r_3(x/t)]^2, \\
 \lambda_2(x/t) &= \frac{1}{16}[4\sqrt{\rho_0} + 2 - r_3(x/t)]^2, \\
 \lambda_3(x/t) &= \frac{1}{16}[4\sqrt{\rho_0} - 2 + r_3(x/t)]^2,
 \end{aligned} \tag{IV.58}$$

where r_3 satisfies the implicit equation (IV.48). For $1 < \rho_0 < 4$, $\sigma(x/t) \equiv 1$. When $\rho_0 \geq 4$, there is a vacuum point and σ is given in equation (IV.56).

Here we find that a key difference between dispersive and dissipative shock waves is the method of regularization. In the dispersive case, we use initial data regularization. In particular we argue that, with the correct choice of initial data, the hyperbolic Whitham equations have a smooth solution for all time. Whereas in the dissipative case, jump/entropy conditions are employed. Using a dispersive regularization, we have determined the behavior of a fundamental DSW in Bose-Einstein condensates. The averaged behavior of the DSW is similar to the classical shock case but the speeds and oscillatory behavior are different.

E. Theoretical Explanation of Experiments

In order to investigate the development of dispersive shock waves in 2D and 1D, we assume that the condensate is “prepared” by the 3D evolution, using the results of the two experiments with the potentials V_{it} (eq. (III.1)) and V_{ot} (eq. (III.2)). The state of the condensate at a specific time, $t = \tilde{t}$ (described later), is used as an initial condition for a new set of equations in one and two dimensions

$$\begin{aligned}
 \text{2D: } \Psi_{2D}(\rho, t = 0) &= \Psi(\rho, z = 0, t = \tilde{t}) \\
 \text{1D: } \Psi_{1D}(x, t = 0) &= \Psi(x, z = 0, t = \tilde{t}), \quad x \geq 0 \\
 \Psi_{1D}(-x, t = 0) &= \Psi_{1D}(x, t = 0).
 \end{aligned} \tag{IV.59}$$

Because the anti-trap term in the potentials V_{it} and V_{ot} mainly serves to speed up condensate expansion, we neglect this term ($\alpha_r = 0$) when comparing the differing dimensional problems. In Fig. 23 the difference between $\alpha_r \neq 0$ and $\alpha_r = 0$ can be seen. Specifically, we solve the following three equations numerically in three, two, and one dimensions respectively

$$\begin{aligned}
 i\varepsilon \frac{\partial \Psi_{3D}}{\partial t} &= -\frac{\varepsilon^2}{2} \left(\frac{\partial^2 \Psi_{3D}}{\partial r^2} + \frac{1}{r} \frac{\partial \Psi_{3D}}{\partial r} + \frac{\partial^2 \Psi_{3D}}{\partial z^2} \right) \\
 &\quad + \frac{1}{2} \alpha_z z^2 \Psi_{3D} + |\Psi_{3D}|^2 \Psi_{3D} \\
 i\varepsilon \frac{\partial \Psi_{2D}}{\partial t} &= -\frac{\varepsilon^2}{2} \left(\frac{\partial^2 \Psi_{2D}}{\partial r^2} + \frac{1}{r} \frac{\partial \Psi_{2D}}{\partial r} \right) + |\Psi_{2D}|^2 \Psi_{2D} \\
 i\varepsilon \frac{\partial \Psi_{1D}}{\partial t} &= -\frac{\varepsilon^2}{2} \frac{\partial^2 \Psi_{1D}}{\partial x^2} + |\Psi_{1D}|^2 \Psi_{1D},
 \end{aligned} \tag{IV.60}$$

with the initial conditions given in (IV.59) and $\Psi_{3D}(r, z, t = 0) = \Psi(r, z, t = \tilde{t})$.

Comparison of the numerical simulations in different dimensions is made by considering the density $|\Psi|^2$ and the appropriate velocity of Ψ . In 3D the radial velocity is defined to be $[\arg \Psi_{3D}(r, 0, t)]_r$. In 2D, the velocity is $[\arg \Psi_{2D}(r, t)]_r$ whereas in 1D, the velocity is $[\arg \Psi_{1D}(x, t)]_x$. The 3D and 2D results are found to be barely distinguishable with less than 1% difference between them in density, the difference between them cannot be seen in Fig. 23. Also, in Figs. 24 and 27, it is

shown that the three dimensional and one dimensional results are qualitatively the same hence the analytical studies in 1D in section IV D are reasonable approximations of the 3D case.

First we consider the in trap simulation with the potential V_{it} (eq. (III.1)). We take the state of the condensate at time $\tilde{t} = \delta t$ (5 ms), just after the laser has been applied. Now, the evolution is governed solely by the GP equation with an expansion potential. Figure 23 is a comparison between the 3D evolution with ($\alpha_r = 0.71$) and without ($\alpha_r = 0$) the expansion potential. The trailing edge of the DSW propagates towards the center when there is no expansion potential whereas in the full simulations with the expansion potential, both the leading and trailing edges of the DSW propagate radially outward. Otherwise, the two simulations are very similar. In order to investigate dispersive shock behavior, we neglect the expansion potential, $\alpha_r = 0$ from now on. We refer to this case as the modified in trap experiment.

The evolution in Fig. 23 shows the development of a DSW on the inner ring of high density and another DSW on the outer edge of the ring. The density is given on the left while the radial velocity is plotted on the right. The outer DSW (see $t = 2.8$ ms) loses its strength and vanishes. The DSW shock structure investigated in the previous section can clearly be seen in the radial velocity plot (compare with the asymptotic solution in Fig. 21). The appearance of a vacuum point is clear in the velocity plot as well.

In Fig. 24, the 3D simulation of the modified in trap experiment is compared with the corresponding 1D simulation. Both depict the generation of DSWs and we see that they are in good qualitative agreement. The 1D density grows to about twice the magnitude of the 3D density. In the velocity plot, the 3D DSW speeds (trailing and leading) are faster than the 1D speeds. Therefore, the 1D analysis performed in section IV D is applicable to this 3D experiment only in a qualitative sense—it explains the basic structure of a DSW in 3D.

As outlined in section IV, dissipative and dispersive shock waves have quite different properties. In Fig. 25, 2D simulations of the Euler equations of gas dynamics and a BEC are compared. The dissipative regularization of the Euler equations was calculated using the finite volume package Clawpack [17] for the conservation laws

$$\begin{aligned} \rho_t + (\rho u)_r + \frac{\rho u}{r} &= 0 \\ (\rho u)_t + (\rho u^2 + \frac{1}{2}\rho^2)_r + \frac{\rho u^2}{r} &= 0. \end{aligned} \quad (\text{IV.61})$$

The same initial conditions for both the dissipative and dispersive cases were used. Both simulations depict the generation of two shock waves, one on the inner edge of the high density ring and another on the outer edge. The outer shock vanishes in both cases as it propagates into the region of negligible density. Recall that a shock wave can only exist when there is a non-zero density on both of its sides [17]. As we have shown, the dissipative

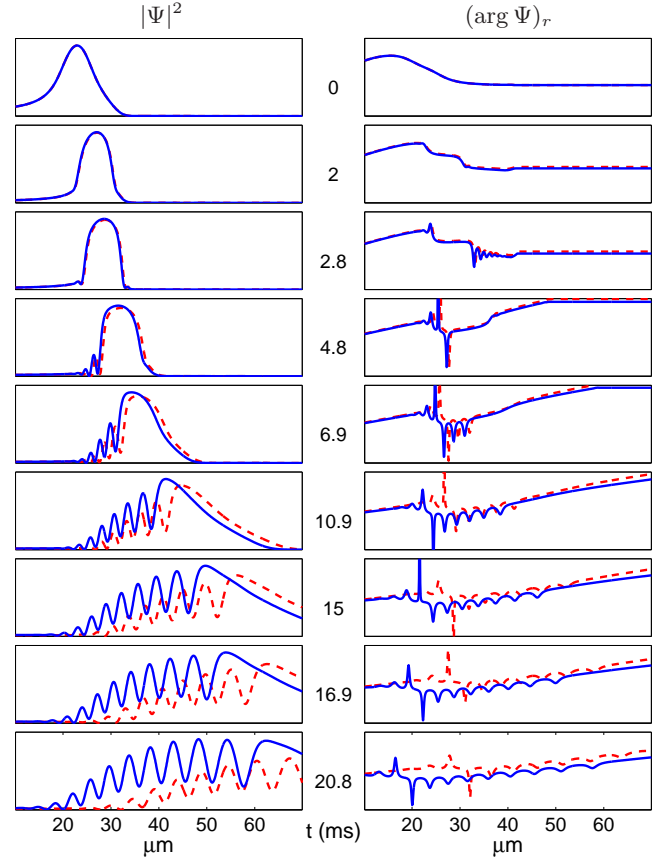


FIG. 23: Development and propagation of DSW in the 3D in trap experiment with (dashed) and without (solid) the expansion potential. The expansion potential does not alter the structure of the DSW, just the speeds. The 3D and 2D densities are in excellent agreement with a maximum relative error of less than 1%. The difference cannot be seen in this graphic.

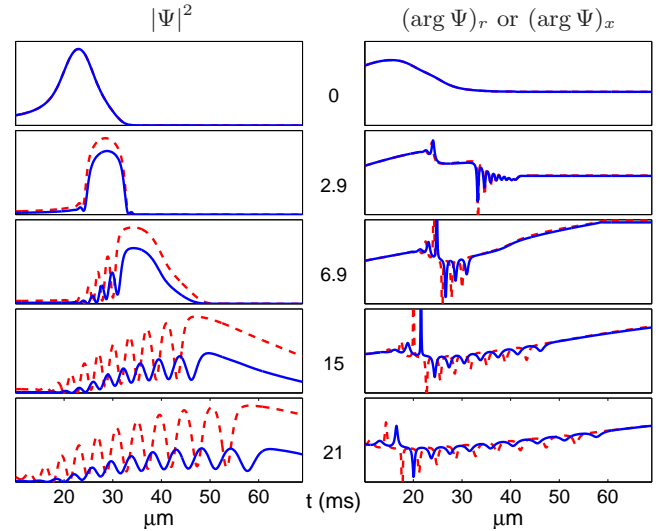


FIG. 24: Comparison of 3D $\Psi_{3D}(r, z = 0, t)$ (solid) and 1D $\Psi_{1D}(x, t)$ (dashed) simulations of DSW in the modified in trap experiment showing good qualitative agreement.

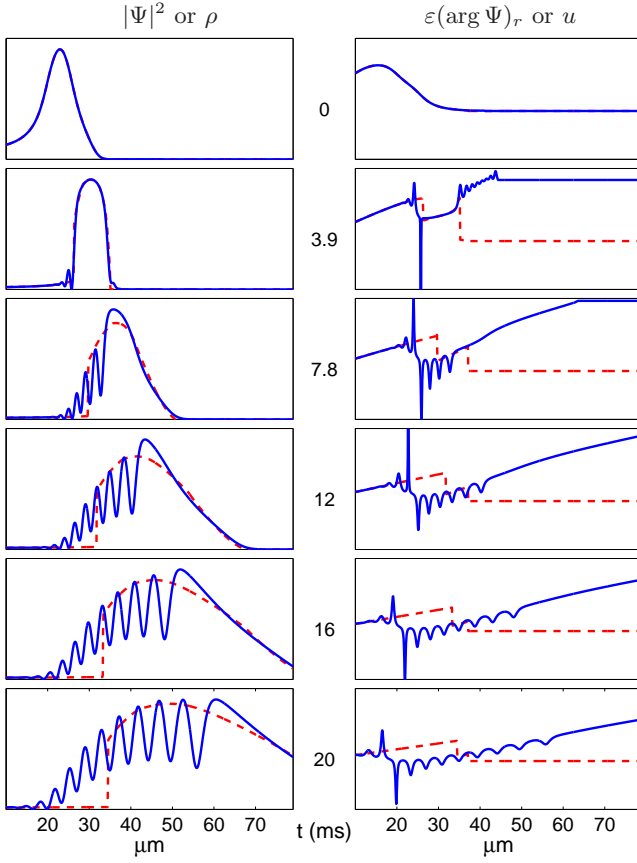


FIG. 25: Comparison of 2D simulations for BEC (solid) and gas dynamics (dashed). The dissipative regularization used in the gas dynamics simulation was calculated using Clawpack [17].

and dispersive shocks propagate with different speeds. However, the densities in the two simulations do agree in regions not affected by breaking, the smooth region to the right of the DSW. As discussed in the previous section, the dissipative and dispersive regularizations are the same when there is no breaking.

For the out of trap experiment, we consider the state of the condensate at time \tilde{t} corresponding to about 10 ms during the experiment or 1 ms after the laser has been turned on. This particular \tilde{t} was chosen because it represents the time just before breaking occurs in the experimental simulations (see Fig. 5). As in the previous simulations, we neglect the expansion potential ($\alpha_r = 0$) in V_{ot} (III.2).

In Fig. 26, the development and interaction of two DSWs is shown from the evolution of the density $|\Psi_{3D}(r, 0, t)|^2$ and the radial velocity $[\arg \Psi_{3D}(r, 0, t)]_r$. The signatures of two DSWs (Fig. 12) are easier to see in the velocity plots on the right of Fig. 26 as the density modulations are large. At $t = 0.13$ ms, two DSWs begin to develop on the inner and outer sides of the high density ring. At $t = 0.33$ ms, these two DSWs begin to interact giving rise to doubly periodic or multi-phase be-

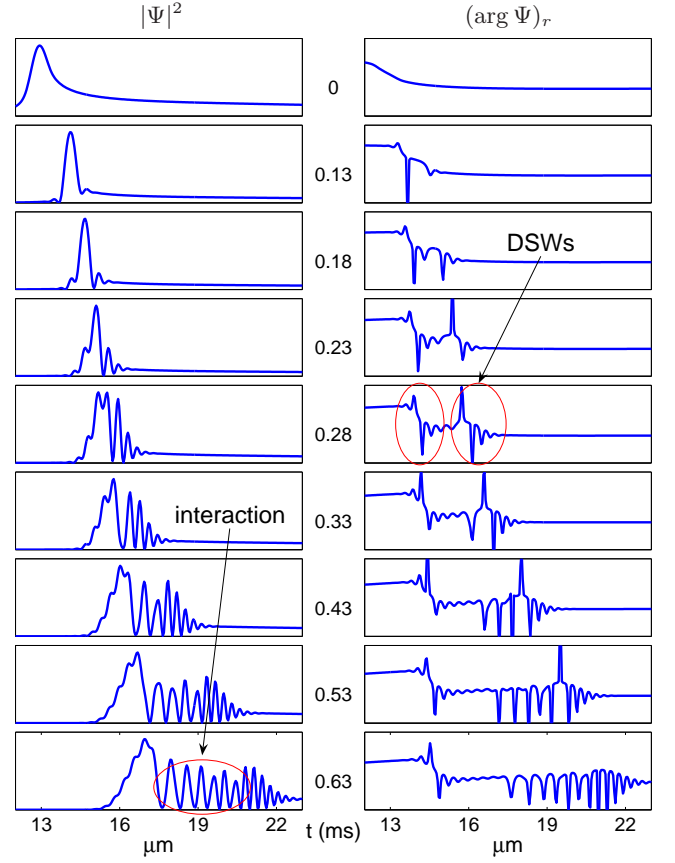


FIG. 26: Three dimensional shock development and interaction for the modified out of trap experiment. The left plot shows the evolution of the density $|\Psi(r, 0, t)|^2$ and the right plot shows the evolution of the radial velocity $[\arg \Psi(r, 0, t)]_r$, both in the $z = 0$ plane. As with the in trap experiment, the maximum absolute difference in density from the 2D evolution has a relative error of less than 1%.

havior. Following this, a DSW front propagates ahead of the interaction region. We will examine this interaction behavior in more detail in the future.

In Fig. 27, the 3D and 1D simulations are compared for the modified out of trap experiment. The agreement is quite good over the short time scale considered (1 ms). This shows that the *initial* generation and interaction of DSWs in 3D BECs is well explained by the 1D approximation. At later times it is found that the amplitudes and speeds diverge roughly similar to what we saw in Fig. 24

Figure 28 shows a comparison of the dissipative regularization of the 2D Euler equations (IV.61) and the dispersive regularization given by the small dispersion limit of the Gross-Pitaevskii equation (IV.60). The dissipative regularization was calculated using Clawpack [17]. As in the dispersive case, the gas dynamics equations develop two shock waves on the inner and outer sides of the ring. The inner shock wave propagates as long as there is non-zero density on its inner edge. This be-

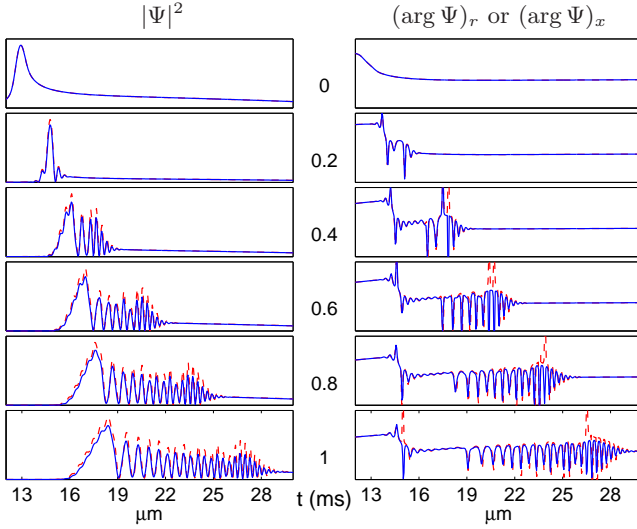


FIG. 27: Comparison of 3D (solid) and 1D (dashed) shock development. The left plot shows evolution of density; the right plot shows the evolution of the velocity. There is good qualitative agreement over this short time scale.

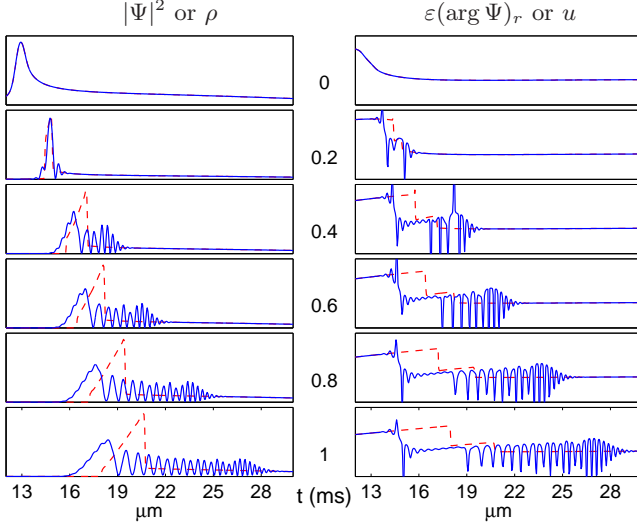


FIG. 28: Shock evolution in 2D BEC (solid) and the dissipative regularization of the 2D Euler equations (dashed). The left plot is density and the right plot is radial velocity. The dissipative regularization was calculated using Clawpack [17].

havior is predicted by the 1D analysis where, with zero background density, the solution is always a rarefaction (expansion) wave. The structure and speeds of the two types of shocks are quite different as expected from the analysis given in this work.

V. CONCLUSION

We have presented new experimental evidence for dispersive shock waves (DSWs) in a Bose-Einstein condensate. Numerical simulations of the experiments and comparisons with lower dimensional approximations show that the experimentally observed ripples correspond to DSWs. A DSW has two associated speeds (front and rear of the oscillatory region) and large amplitude oscillatory structure.

A detailed comparison between classical, dissipative shock waves and dispersive shock waves has been undertaken in this work. On a large scale, a DSW has some similarities to a dissipative shock, but there are fundamental and critical differences. Using the notions of averaging and weak limits, we have shown that a DSW has one behavior similar to that of a classical shock—i.e. it has a steep front. However, the key difference between a DSW and a dissipative shock is in the shock speed and its structure. These properties are compared using dissipative and dispersive regularizations of conservation laws. A dispersive regularization for conservation laws gives rise to a *weak* limit in the sense that one must appropriately average over the high frequency oscillations across a DSW. On the other hand, a dissipative regularization for conservation laws is a strong limit which, in the case of a classical shock wave, converges to a discontinuity propagating with a speed that satisfies the well known jump conditions.

Acknowledgments

This work was supported by NSF grants DMS-0303756 and VIGRE DMS-9810751. The experimental part of this work was funded by NSF and NIST.

-
- [1] R. Courant and K. O. Friedrichs, *Supersonic Flow and Shock Waves* (Springer-Verlag, 1948).
 - [2] Z. Dutton, M. Budde, C. Slowe, and L. V. Hau, *Science* **293**, 663 (2001).
 - [3] T. P. Simula *et al.*, *Phys Rev Lett* **94**, 080404 (2005).
 - [4] M. Zak and I. Kulikov, *Phys Lett A* **307**, 99 (2003).
 - [5] B. Damski, *Phys Rev A* **69**, 043610 (2004).
 - [6] A. M. Kamchatnov, A. Gammal, and R. A. Kraenkel, *Phys Rev A* **69**, 063605 (2004).
 - [7] F. K. Adbullaev, A. Gammal, A. M. Kamchatnov, and

- L. Tomio, *Int J Mod Phys B* **19**, 3415 (2005).
- [8] C. J. Pethick and H. Smith, *Bose-Einstein Condensation in Dilute Gases* (Cambridge University Press, 2002).
- [9] W. Bao, D. Jaksch, and P. A. Markowich, *J Comput Phys* **187**, 318 (2003).
- [10] S. Jin, C. D. Levermore, and D. W. McLaughlin, in *Singular Limits of Dispersive Waves*, edited by N. M. Ercolani *et al.* (Plenum Press, 1994), vol. 320, pp. 235–255.
- [11] H. W. Liepmann and A. Roshko, *Elements of Gasdynamics* (Wiley, 1957).

- [12] I. Coddington et al., Phys Rev A **70**, 063607 (2004).
- [13] Z. H. Musslimani and J. Yang, J Opt Soc Am B **21**, 973 (2004).
- [14] B. Fornberg, *A Practical Guide to Pseudospectral Methods* (Cambridge University Press, 1998).
- [15] P. D. Lax, *Hyperbolic systems of conservation laws and the mathematical theory of shock waves* (SIAM, 1973).
- [16] P. G. LeFloch, *Hyperbolic Systems of Conservation Laws* (Birkhäuser, 2002).
- [17] R. J. LeVeque, *Finite Volume Methods for Hyperbolic Problems* (Cambridge University Press, 2002).
- [18] C. S. Gardner and G. K. Morikawa, Tech. Rep. NYO 9082, Courant Institute of Mathematical Sciences (1960).
- [19] G. B. Whitham, Proc Roy Soc Ser A **283**, 238 (1965).
- [20] A. V. Gurevich and L. P. Pitaevskii, Sov Phys JETP **38**, 291 (1974).
- [21] Y. Kodama, SIAM J Appl Math **59**, 2162 (1999).
- [22] P. F. Byrd and M. D. Friedman, *Handbook of Elliptic Integrals for Engineers and Physicists* (Springer-Verlag, 1954).
- [23] L. Debnath, *Nonlinear Partial Differential Equations* (Birkhäuser, 2005).
- [24] D. Levermore, Commun Part Diff Eq **13**, 495 (1988).
- [25] M. J. Ablowitz and H. Segur, Stud Appl Math **57**, 13 (1977).
- [26] C. S. Gardner, J. M. Greene, M. D. Kruskal, and R. M. Miura, Phys Rev Lett **19**, 1095 (1967).
- [27] C. S. Gardner, J. M. Greene, M. D. Kruskal, and R. M. Miura, Comm Pur Appl Math **27**, 97 (1974).
- [28] P. Lax and C. Levermore, Comm Pur Appl Math **36**, 253, 571, 809 (1983).
- [29] A. V. Gurevich and A. L. Krylov, Sov Phys JETP **65**, 944 (1987).
- [30] G. A. El, V. V. Geogjaev, A. V. Gurevich, and A. L. Krylov, Physica D **87**, 186 (1995).
- [31] G. Biondini and Y. Kodama, nlin.SI/0508036 (2005).
- [32] M. J. Ablowitz and H. Segur, *Solitons and the Inverse Scattering Transform* (SIAM, 1981).
- [33] M. V. Pavlov, Teor Mat Fiz **71**, 351 (1987).
- [34] M. G. Forest and J. Lee, in *Oscillation Theory, Computation, and Methods of Compensated Compactness*, edited by C. Dafermos et al. (Springer, 1986), vol. 2, pp. 35–69.